Biomolecular Controls on Calcium Carbonate Formation by Classical and Amorphous Pathways: Insights from Measurements of Nucleation Rates and Isotope Tracers

Anthony Joseph Giuffre

Dissertation submitted to the faculty of the Virginia Polytechnic Institute and State University in partial fulfillment of the requirements for the degree of

Doctor of Philosophy
In
Geosciences

Patricia M. Dove, chair
J. Donald Rimstidt
Michael F. Hochella, Jr.
Maren Roman
James J. De Yoreo

March 4th, 2015
Blacksburg, VA

Keywords: biomineralization, kinetics, polysaccharides, surface energy, paleoclimate proxy models

BIOMOLECULAR CONTROLS ON CALCIUM CARBONATE FORMATION BY CLASSICAL AND AMORPHOUS PATHWAYS: INSIGHTS FROM MEASUREMENTS OF NUCLEATION RATES AND ISOTOPE TRACERS

Anthony J. Giuffre

ABSTRACT

Calcified skeletons are produced within complex assemblages of proteins and polysaccharides whose roles in mineralization are not well understood. Researchers have long postulated that living organisms utilize the macromolecules of organic matrices to actively guide the formation of crystal structures. The timing and placement of the subsequent minerals that form are most easily controlled during nucleation; however, a physical and chemical picture of how organic functional group chemistry influences the initial stages of nucleation is not yet established. These processes are further complicated by the realization that carbonate biominerals can form by an amorphous to crystalline transformation process, which has prompted the question of how chemical signatures are recorded during mineralization. Investigations of mineralization processes such as the kinetics of nucleation and the transformation of amorphous calcium carbonate (ACC) to crystalline products are critical to building a better understanding of biomineral formation. Only from that fundamental basis can one begin to decipher changes in climate and seawater chemistry over geologic time and by recent anthropogenic effects.

This dissertation presents the findings from experimental studies of the thermodynamics and kinetics of multiple mineral formation processes, including nucleation and transformation from an amorphous phase. The kinetics of calcite nucleation onto a suite of high-purity polysaccharide (PS) substrates were quantified under controlled conditions. Nucleation rates were measured as a function of 1) supersaturation extending above and below ACC solubility and 2) ionic strength extending to seawater salinity. These conditions decipher the chemical interactions between the PS substrate, calcite crystal, and solution. These investigations show the energy barrier to calcite formation is regulated by competing interfacial energies between the substrate, crystal, and liquid. The energy barriers to nucleation are PS-specific by a systematic relationship to PS charge density and substrate structure that is rooted in minimization of the competing substrate–crystal and substrate–liquid interfacial energies. The data also suggest ionic strength regulates nucleation barriers through substrate-liquid and crystal-liquid interfacial energetics.

In a second experimental study, stable isotope labeling was used to directly probe the transformation pathway. Four processes were considered: dissolution-reprecipitation, solid-state, or combinations of these end member processes. Isotope measurements of calcite crystals that transform from ACC have signatures that are best explained by dissolution-reprecipitation. The extent of isotopic mixing correlates with the amount of ACC transferred and the time to transformation, suggesting the calcite crystals are recording the changing local solution environment during the transformation. These investigations into different mineralization mechanisms build a framework for how functional group chemistries of organic molecules regulate mineralization and the resulting isotopic and elemental signatures in the calcite. This may provide useful insights to interpreting chemical signatures of carbonate biominerals in fossil record and understanding ocean chemistry changes throughout geologic time.

ACKNOWLEDGEMENTS

To my advisor Patricia Dove, I thank you for your support, leadership, and guidance in becoming a better scientist. Your access to resources and insightful and honest discussions have provided an invaluble and fulfilling academic experience. You have provided endless advice, allowed my goals and growth to take priority, and kept me grounded in reality. You have ensured I will thrive as a careful scientist who always has access to the "clue card" to ask directed questions and make quantitative measurements that can provide answers to big problems. Thank you for your patience, understanding, and support over the last six years.

To Jim De Yoreo, thank you for your invested interest in my research and for providing access to resources, techniques, and analyses that have served as the basis for each of my projects. Your endless advice and insights in interpreting data and writing manuscripts have been critical to the success of these projects. To Mike Hochella, thank you for your support and for providing a broad perspective when I fixated on the details. To Don Rimstidt, thank you for brainstorming project ideas and technical solutions to experimental set-backs, and for providing critical feedback on manuscripts. To Maren Roman, thank you for your insights and expertise on polysaccharide chemistry and characterization techniques. To my collaborators, Alex Gagnon, Jinhui Tao, Debin Wang, Laura Hamm, Dongbo Wang, and especially Nizhou Han, I thank you for your technical expertise, mentorship, and patience that I will surely try to model in future collaborations.

To faculty at VT, Kevin Edgar, Johan Foster, William Ducker, Pete Vikesland, for providing critical information and resources needed to push my research past the boundaries of geosciences. To Sebastian Mergelsberg, Christina Blue, Adam Angel, Laura Hamm, Dongbo Wang, Adam Wallace, Laura Wasylenki, Rebecca French, Carol Johnson, Harish Veeramani, Jie Xu, James Dale, Sarah Ulrich, and other members of the Dove and Hochella groups, thank you for your patience, encouragement, countless conversations, and endless advice about graduate school and research problems. I am more than certain I could not have succeeded without your diverse perspectives, support, and camaraderie.

Thank you to staff and graduate students of geosciences department at VT, in particular Connie Lowe, Mary McMurray, Sharon Collins, Jo Thomason, Ellen Mathena, Llyn Sharp, Jim Langridge and Mark Lemon. Thank you to all of my friends at VT and around the world: T.J. Metzger, Allan Paquette, Kati Paquette, Randi Hagen, Erica Hagen, Chris Schubert, Rachel Saeman, Laura Halvorson, Tristan Halvorson, Will McCardell, Sarah Mazza, Sarah Timm, Eric Christensen, John Wyatt, Aaron Refflet, Lindsay Kolbus, Majken Schimmel, Marilyn Duncan, Troy Dexter, Matt Chan, Becky Lahr, Nina Vance, Andrea Tiwari, Ariel Conn, Ryan Capobianco, Hector Lamadrid, Ken O'Donnell, Jesse Broce, Mike Meyers, Jenn Sliko Meyer, Drew Hawkins, Pavithra Sekhar, Aida Farough, Matt MacInnis, Pilar Lecumberri.

To my partner Carrie Tyler, thank you for your mentorship in navigating the world of academia, for always believing I could succeed, and for providing endless encouragement. To my siblings Carl, Mary, Jon, and Laura, and to my parents Lee, Alan, and Patty, thank you for getting me back on my feet with your enduring support and for your sincere enthusiasm in my work.

ATTRIBUTIONS

Chapter 2:

Laura M. Hamm, Ph.D., is a co-author on this paper and helped with designing the flow-through apparatus, optimizing experimental parameters, and establishing groundwork for classical nucleation theory.

Nizhou Han, Ph.D., is a research scientist in the Geosciences department at Virginia Tech and is a co-author on this paper, helped with designing the flow-through apparatus and optimizing experimental parameters.

James J. De Yoreo, Ph.D., is the Chief Scientist for the Materials Synthesis and Simulation Across Scales group at Pacific Northwest National Laboratory and an affiliate professor of Materials Science and Engineering at the University of Washington. Dr. De Yoreo is a co-author on this paper and helped with designing the project, analyzing the nucleation rate and surface energy measurements, establishing groundwork for classical nucleation theory, and writing the paper.

Patricia M. Dove, Ph.D., is a University Distinguished Professor and C.P. Miles Professor of Science in the Geosciences department at Virginia Tech. Dr. Dove is a co-author on this paper and helped with designing the project, analyzing the nucleation rate and surface energy measurements, establishing groundwork for classical nucleation theory, and writing the paper.

Chapter 3:

Alexander C. Gagnon, Ph.D., is an Assistant professor in the Chemical Oceanography department at the University of Washington. Dr. Gagnon is a co-author on this paper and provided enriched isotope solutions, helped with designing the project, performing the sample preparation and analyses on NanoSIMS and Q-ICP-MS, interpretating the data, building the mixing model, and writing the paper.

James J. De Yoreo, Ph.D., is the Chief Scientist for the Materials Synthesis and Simulation Across Scales group at Pacific Northwest National Laboratory and an affiliate professor of Materials Science and Engineering at the University of Washington. Dr. De Yoreo is a co-author on this paper and helped with designing the project, interpreting the data, and writing the paper.

Patricia M. Dove, Ph.D., is a University Distinguished Professor and C.P. Miles Professor of Science in the Geosciences department at Virginia Tech. Dr. Dove is a co-author on this paper and helped with designing the project, interpreting the data, and writing the paper.

TABLE OF CONTENTS

ABSTRACT ..... **ii**
ACKNOWLEDGEMENTS ..... **iii**
ATTRIBUTIONS ..... **iv**
LIST OF FIGURES ..... **vii**
LIST OF TABLES ..... **viii**
PREFACE ..... **ix**
CHAPTER 1. INTRODUCTION **1**
1.1. MOTIVATION FOR STUDY 1
1.2. PRIOR FOCUS ON PROTEINS OVER POLYSACCHARIDES 3
1.3. INSIGHTS FROM CLASSICAL NUCLEATION THEORY 4
1.4. FUTURE WORK: EFFECTS OF IONIC STRENGTH ON NUCLEATION 6
1.5. REFERENCES 9
CHAPTER 2. POLYSACCHARIDE CHEMISTRY REGULATES KINETICS OF CALCITE NUCLEATION THROUGH COMPETITION OF INTERFACIAL ENERGIES **11**
2.1. ABSTRACT 11
2.2. INTRODUCTION 12
2.3. MATERIALS AND METHODS 15
2.3.1. Preparation of PS films 15
2.3.2. Measurement of nucleation rates 16
2.3.3. Measurements of surface free energy 17
2.4. RESULTS AND DISCUSSION 17
2.5. IMPLICATIONS 24
2.6. REFERENCES 26
CHAPTER 3: ISOTOPIC TRACER EVIDENCE FOR THE AMORPHOUS CALCIUM CARBONATE TO CALCITE TRANSFORMATION BY DISSOLUTION-REPRECIPITATION **29**
3.1. ABSTRACT 29
3.2. INTRODUCTION 30
3.3. METHODS 34
3.3.1. Synthesis of ACC and transformation to calcite 34
3.3.2. Isotope labeling using ^{43}Ca and ^{25}Mg 35
3.3.3. Experimental design 36
3.3.4. NanoSIMS spot analysis 38
3.4. RESULTS 41
3.4.1. ACC precipitation and transformation to Mg-calcite 41
3.4.2. Isotopic analysis of controls and treatments 43
3.5. DISCUSSION 47
3.5.1. Transformation pathways and mixing model 47
3.5.2. Qualitative insights for the transformation process 50
3.5.3. Implications 52
3.6. REFERENCES 55
APPENDIX A. SUPPLEMENTARY INFORMATION FOR CHAPTER 1 ..... **59**
A1. SIZE AND POLYDISPERSITY OF POLYSACCHARIDES 59

A2. ELECTROPHORETIC MOBILITY AND ZETA POTENTIAL OF PS 61
A3. POTENTIOMETRIC TITRATION OF PS 62
A4. EFFECT OF IONIC STRENGTH ON HETEROGENEOUS NUCLEATION 65
A5. EFFECT OF IONIC STRENGTH ON HOMOGENEOUS NUCLEATION..... 68
A6. REFERENCES 72
APPENDIX B. SUPPLEMENTARY INFORMATION FOR CHAPTER 2 73
B1. MEASUREMENTS OF SURFACE FREE ENERGY 73
B2. CLASSICAL NUCLEATION THEORY 75
B3. CALCULATION OF CHARGE FROM ACID DISSOCIATION CONSTANTS 76
B4. CALCULATION OF CHARGE DENSITY OF SAM AND PS SUBSTRATES. 78
B5. ADDITIONAL TABLES OF DATA..... 79
B6. REFERENCES..... 80
APPENDIX C. SUPPLEMENTARY INFORMATION FOR CHAPTER 3 82
C1. ADDITIONAL TABLES OF DATA..... 82
C2. HYPERBOLIC BINARY MIXING MODEL 83
C3. REFERENCES..... 84

LIST OF FIGURES

Fig. 2.1: Polysaccharide chemical structures illustrate the functional groups attached to 2-carbon (red) and 6-carbon (blue) of each ring. 14
Fig. 2.2: Calcite steady-state nucleation rates obey classical nucleation theory (Eq. 2.2) and show PS-specific dependence on B, a proxy for the thermodynamic barrier to nucleation. 18
Fig. 2.3: Kinetic measurements provide insights to controls on thermodynamic barriers to nucleation. 20
Fig. 3.1: Experimental design for ^{43}Ca and ^{25}Mg isotope labeling of solutions and solid phases. 37
Fig. 3.2: SEM images of representative calcite morphologies. 42
Fig. 3.3: Typical NanoSIMS spot analysis show the typical isotope counts collected over 60 cycles of measurements for two high-Mg calcite crystals 44
Fig. 3.4: The isotope ratios determined from calcites for the natural abundance controls (blue squares), the spiked controls (red triangles), and experimental treatments that began as ACC in natural abundance solutions and were transferred to spiked solutions for transformation to calcite (green circles). 46
Fig. 3.5: Predictions of mixing model show isotope-specific signatures expected for calcite that transforms from ACC 49
Fig. A.1: Measurements of alginate alginate (red) and chitosan (purple) as a function of ionic strength using dynamic light scattering show a decreasing trend in PS diameter (Z-ave) and PS dispersion in size (PDI). 60
Fig. A.2: Electrophoretic mobility measurements and zeta potential calculations for chitosan (purple) and alginate (red) show trends that indicate the mobility and charge of PS decreases in higher ionic strength solutions. 62
Fig. A.3: Potentiometric titration curves for A) alginate and B) chitosan at varying ionic strength from ~0 to 600 mM. 64
Fig. A.4: Potentiometric titrations of chitosan and alginate have no apparent trend in calculated number of charged groups with varying ionic strength. 65
Fig. A.5: Linearized function of heterogeneous nucleation rates of calcite onto two polysaccharide substrates 66
Fig. A.6: Energy barriers to nucleation, B, are greater with increasing ionic strength for both alginate (red) and chitosan (purple). 67
Fig. A.7: Example of measurements of pH and $[Ca^{2+}]$ in a homogeneous nucleation experiment. 70
Fig. A.8: Homogeneous nucleation experiments show a decrease in induction time with higher supersaturation and higher ionic strength. 70
Fig. B.1: Contact angle measurements determine the surface free energy in air (gS-air) of polysaccharide substrates by the relationship in **Eq. (A9)**. 74

LIST OF TABLES

Table 2.1: Examples of polysaccharides found at sites of $CaCO_3$ mineralization from diverse phyla. 13
Table 3.1: Summary of solution isotope enrichments..... 36
Table 3.2: The Mg content (mol% $MgCO_3$) of calcite averaged across all isotope conditions..... 40
Table A.1: PS diameter (Z-ave) and PS dispersion in size (PDI) are shown for alginate and chitosan as a function of ionic strength..... 60
Table A.2: Measurements of PS electrophoretic mobility, μ_E, and calculated zeta potential, ζ, are shown for alginate and chitosan as a function of ionic strength. 62
Table A.3: Summary of solution compositions and supersaturation used in nucleation experiments onto alginate and chitosan at varying ionic strength. 67
Table A.4: Nucleation rates of calcite onto alginate and chitosan at varying ionic strength. Rates are normalized to 1.23 mm^2 viewing area of optical microscope. 68
Table A.5: Proxy for the thermodynamic barrier to nucleation, B, is derived from slopes of linear trends in **Fig. A.5** and from data in **Table A.4**..... 68
Table A.6: Induction time to homogeneous nucleation is shown as a function of ionic strength and supersaturation with respect to calcite. 71
Table B.1: Summary of surface free energy and its polar and dispersive components from OWRK calculations. 75
Table B.2: Estimates of charge using acid dissociation constants of organic acids that represent different functional groups on the polysaccharide. 78
Table B.3: Summary of solution compositions and supersaturation used in nucleation experiments onto PS substrates..... 79
Table B.4: Nucleation rates of calcite onto PS substrates in 1.23 mm^2 viewing area of optical microscope over the course of experiment. 80
Table B.5: Proxy for the thermodynamic barrier to nucleation, B, is derived from slopes of linear trends in **Fig. 2.2** and from data in **Table B.4**..... 80
Table C.1: Summary of isotope ratio measurements shown in **Fig. 3.4**..... 82
Table C.2: Hyperbolic mixing model coefficients are calculated from Mg content and isotopic composition of ACC and solution according to **Eq. C.1** and **Eq. C.2**..... 84

PREFACE

This dissertation is organized into three chapters. Chapter 1 introduces the motivation for the research but it is not a published manuscript. The subsequent chapters are presented as manuscripts in various stages of publication or preparation. Chapter 2 is published in *Proceedings for the National Academy of Sciences* in 2013. Chapter 3 is currently under peer review for *Geochimica et Cosmochimica Acta.*

CHAPTER 1. INTRODUCTION

1.1. MOTIVATION FOR STUDY

Organic-mineral composites known as biominerals have been utilized by many organisms throughout Earth's history and today to build shells, skeletons, and tissues with complex yet precise structure and function. Because these resilient materials are well-preserved in the fossil record, the macroscopic features of biominerals have recorded the evolution of predation strategies and defense mechanisms for ancient marine organisms. Biominerals have also provided critical, high resolution chemical and isotopic records of ancient climate conditions and seawater chemistry using empirical calibrations with modern organisms. Despite the significance of biomineralized structures in understanding evolution of life and changes in climate over geologic time, the concerted biochemical processes that govern how organisms build their shells and skeletons remain enigmatic.

Organisms invest extenstive effort and energy in controlling precisely where, when, and how their shells and skeletons form. Controls over timing, for example are governed by enhancing and inhibiting nucleation and growth rates. The location of mineral formation is governed by some combination of 1) lipid and cell surface chemistry; 2) organic matrix chemistry, usually a gel-like framework made of proteins and polysaccharides; and/or 3) mineralizing fluids rich in small, soluble organic molecules. This leads to the question of how general are the chemical and physical roles of organic molecules in biomineralization of the shells and skeletons of organisms across the phylogenetic tree?

Mineralization processes are dependent upon a number of properties of the surrounding environment, including: solution chemistry, saturation state of the mineral,

inorganic ions, ionic strength, pH, Eh, temperature, soluble organics, and insoluble organics as gels or substrates. These properties are interrelated and many of them are strictly regulated by organisms inside and outside of cells at the site of mineralization. Thus, both the local chemistry as well as the larger biochemical cellular processes must be understood to build a complete picture.

Recently, in vivo and in vitro studies have realized crystal growth can occur by processes other than the classical ion-by-ion addition. One crucial unanswered question is whether the chemical and isotopic signatures used as environmental proxies are recorded first in the initial amorphous phase and then transferred to the final crystalline product. If so, this would suggest that many carbonate biomineral-based geochemical proxies reflect the local conditions at the time of amorphous calcium carbonate (ACC) formation. The question of when and where chemical signatures are recorded during calcification by an ACC intermediate has particular significance for efforts to reconstruct paleoenvironmental conditions from the composition and isotopic signals, or proxies, contained in biominerals.

Patterns in the types of biomineralization processes that are found in organisms may provide insights to evolutionary relationships and the biochemical origins of biomineral formation over earth's history (Knoll, 2003). Many organisms use specialized cells or vesicles for mineral formation but the processes and conditions required for forming minerals can vary across phyla and between species. For example, foraminifera tests are either mineralized extracellularly within an organic matrix composed of sulfated glycosaminoglycans (Bé et al., 1963; Bé et al., 1979), or produced in vesicles inside a cell (Hemleben et al., 1986; Weiner et al., 2011). While these two types of foraminifera share

a recent common ancestor, the biological environments used in mineralizing their tests are quite different. On the other hand, the use of sulfated glycosaminoglycans at sites of mineralization can also be found in the matrix of mineralized extracellular sheaths of cyanobacteria (Leak, 1967) and in calcifying fluids of bivalves (Crenshaw, 1972). While many efforts have characterized the organic macromolecules present in biominerals, such as these glycosaminoglycans, the specific roles of their functional groups in mineral formation are largely unknown. Additional research into mineralization processes *in vivo* may reveal patterns across phyla over geologic time. However, the complex and heterogeneous nature of biological systems suggests a need for a chemical framework to explain how organic functional groups regulate mineralization processes.

1.2. PRIOR FOCUS ON PROTEINS OVER POLYSACCHARIDES

Early studies generally assumed that charged acidic proteins are the only macromolecules that can regulate mineralization. This led the biomineralization community to give less attention to polysaccharides (PS), although they are near-ubiquitous in mineralized tissues and are intimately associated with the proteinaceous compounds of the organic matrix. PS such as the chitin found in the insoluble fraction of the mollusk shell are thought to provide an inert scaffolding for these proteins without significant chemical activity (Rudall, 1963; Lowenstam et al., 1989; Weiss et al., 2006). These early interpretations are understandable because polysaccharide compounds are generally considered hydrophobic compared to the "acidic macromolecules" of glycoproteins and/or proteoglycans that have large hydrophilic domains of aspartic and glutamic acids.

The assumption that PS have no role in mineralization is now called into question because of unresolved inconsistencies. Moreover, Furuhashi et al. (2009) argue that

emphasis on acidic proteins has diverted researchers from investigating the roles of other components in mineralization. For example, specific orientations of chitin fibers with neutral functional groups promote the templating of $CaCO_3$ in the lobster carapace (Al-Sawalmih et al., 2008; Giraud-Guille et al., 2004), crab cuticle (Giraud-Guille et al., 2004), and nautilus shell (Nudelman et al., 2006). Furthermore, recent *in vitro* studies recognize that unique properties of PS including branching, monosaccharide sequence, and hydrophobicity can regulate calcite nucleation and growth (Arias et al., 2002; Butler et al., 2006; Arias, 2008; Nielsen et al., 2012; Giuffre et al., 2013; Rao et al., 2014; Sand et al., 2014). Insights from *in vivo* and *in vitro* studies provide evidence that the chemical structure of PS can indeed control calcite nucleation.

1.3. INSIGHTS FROM CLASSICAL NUCLEATION THEORY

The timing of mineral formation in organic matrices is best controlled during nucleation. Classical nucleation theory (CNT) has been recently used to provide insights to thermodynamics of heterogeneous nucleation of calcium carbonate onto a variety of organic films and functionalized substrates (Manoli et al., 1997; Manoli et al., 2000, 2002; Hu et al., 2012; Giuffre et al., 2013; Chevalier, 2014; Hamm et al., 2014; Li et al., 2014). These experimental studies measure mineral nucleation rates, J_0, as a function of chemical driving force or supersaturation, σ, defined as

$$\sigma = \ln \frac{a_{Ca^{2+}} a_{CO_3^{2-}}}{K_{sp}} \qquad [1.1]$$

where a_i are activities of species i and K_{sp} is the equilibrium solubility constant ($10^{-8.48}$ for pure calcite at 25°C). CNT shows J_0 has an exponential dependence upon the energy barrier to nucleation, ΔG,

$$J_0 = A \exp\left(\frac{-\Delta G}{k_B T}\right) \qquad [1.2]$$

where A is a kinetic term that includes ion desolvation and attachment (De Yoreo et al., 2003). The energy barrier, ΔG, is inversely proportional to supersaturation, σ, and directly proportional to the interfacial energy of the nucleating phase, γ, such that:

$$\Delta G = B k_B T \frac{\gamma^3}{\sigma^2} \quad [1.3]$$

where B is a constant that depends on nucleus shape, molecular volume of nucleating phase, Boltzmann's constant, and temperature (**Appendix B**) (De Yoreo et al., 2003; De Yoreo et al., 2013; Giuffre et al., 2013; Hamm et al., 2014). Combining **Eq. 1.2** and **Eq. 1.3** into a linear form, the slope allows the energy barrier to nucleation to be quantified from measured nucleation rates at known supersaturations:

$$\ln (J_0) = \ln(A) - B \left(\frac{1}{\sigma^2}\right) \quad [1.4]$$

As seen in the above relationships, the presence of a surface that reduces the interfacial free energy will promote nucleation by reducing the energy barrier. For heterogeneous nucleation onto a given substrate, γ is controlled by a balance of three interactions – the liquid-crystal (γ_{LC}), substrate-crystal (γ_{SC}) and substrate-liquid (γ_{SL}) interfacial energies:

$$\gamma = \gamma_{LC} + h(\gamma_{SC} - \gamma_{SL}) \quad [1.5]$$

where h is a nucleus shape factor (Hu et al., 2012; Giuffre et al., 2013; Hamm et al., 2014).

Indeed, recent rate measurements confirmed the calcite nucleation barrier is minimized by regulating the interfacial energies of functionalized substrates (Manoli et al., 1997; Manoli et al., 2000, 2002; Hu et al., 2012; Giuffre et al., 2013; Chevalier, 2014; Hamm et al., 2014; Li et al., 2014). Nucleation barriers onto polysaccharide substrates are correlated with charge density such that near-neutral polysaccharides present the lowest

barrier to calcite formation. The near-neutral charge of chitosan favors the formation of a substrate-crystal interface to reduce substrate-water interactions. Progressively higher barriers are measured for negatively charged alginate that favors contact with the solution over the formation of new substrate-crystal interfaces (Giuffre et al., 2013). Thus, the data indicate that substrate-crystal interactions are one end-member in a larger continuum of competing forces that regulate heterogeneous crystal nucleation.

1.4. FUTURE WORK: EFFECTS OF IONIC STRENGTH ON NUCLEATION

To develop a mechanism-based understanding of how macromolecule chemistry regulates nucleation, a complete pictures of substrate-crystal-solution interactions is necessary. Previous work on the heterogeneous nucleation of calcite have not yet resolved the contributions of all three surface energy terms in **Eq. 1.5**. Recall from **Eq. 1.5** that net interfacial energy of a nucleating phase, γ, is dependent upon three terms, two of which involve interactions with the solution (γ_{SL} and γ_{LC}). Larger nucleation barriers are achieved through larger γ of the nucleating system via larger γ_{LC}, larger γ_{SC}, and/or smaller γ_{SL} (**Eq. 1.3 and Eq. 1.5**).

The realization that polysaccharides regulate energy barriers to nucleation by minimizing the competition between interfacial energies leads to the hypothesis that these component terms are significantly dependent upon the composition of the liquid phase. The experimental conditions used in Giuffre et al. (2013) assumed γ_{LC} is approximately constant and has little influence relative to the substrate contributions. However, **Eq. 1.5** suggests there may be situations where this not always be the case and the influence of different solution chemistries on γ_{LC} and γ_{SL} merits further investigation.

Recall that highly charged PS such as alginate have a lower interfacial energy in contact with the solution than neutral PS. Changes in solution chemistry, such as pH or ionic strength, should regulate PS surface charge, chemical speciation, and hydrophilicity through γ_{SL}. Solution conditions may also influence physical properties of PS. For example, when PS are in solutions of low ionic strength, the molecules are physically extended as near-linear chains due to electrostatic repulsion between like charged groups. As the ionic strength is increased, the charges become screened and the PS coils, decreasing the hydrodynamic radius and reducing accessibility of charged groups (Manning, 1969; Cacace et al., 1997; Frank et al., 2003; Xu et al., 2005; Avaltroni et al., 2006; de Kerchove et al., 2006). Ionic strength also affects the structure of PS films. For example, the swelling (hydration) of alginate films decreases with increasing solution ionic strength (de Kerchove et al., 2006). A better understanding of how ions affect the behavior of PS chemical and physical properties may provide insights to how organisms use PS to regulate the timing and placement of calcite during biomineralization.

In an effort to understand these relations, the effects of ionic strength on PS size, charge, and chemical speciation were characterized using dynamic light scattering, zeta potential measurements, and potentiometric titrations (**Fig. A.1, Fig. A.2, Fig. A.3, Fig. A.4**). These characterizations were coupled with heterogeneous nucleation rate measurements of calcite onto alginate and chitosan substrates at variable ionic strength (**Fig. A.5, Fig. A.6**). In another set of experiments, the induction time to homogeneous nucleation of calcite was measured at variable ionic strength to identify the relative contribution of γ_{LC} to the nucleation barrier (**Fig. A.7, Fig. A.8**). Although these characterizations were largely inconclusive and further research into nucleation

experiments is required, the data are presented in **Appendix A**. By investigating the contributions of surface free energies under variable solution conditions, a chemical framework can be established for how organic functional groups regulate the location and timing of mineralization.

1.5. REFERENCES

Arias J.I., Jure C., Wiff J.P., Fernández M.S., Fuenzalida V. and Arias J.L. (2002) Effect of sulfate content of biomacromolecules on the crystallization of calcium carbonate. *Mater. Res. Soc. Symp. Proc.* **711**, HH1.7.1-HH1.7.6.

Arias J.L. (2008) Polysaccharides and proteoglycans in calcium carbonate-based biomineralization. *Chem. Rev. (Washington, DC, U. S.)* **108**, 4475-4482.

Avaltroni F., Seijo M., Ulrich S., Stoll S. and Wilkinson K.J. (2006) Conformational Changes and Aggregation of Alginic Acid as Determined By Fluorescence Correlation Spectroscopy. *Biomacromolecules* **8**, 106-112.

Bé A.W.H. and Ericson D.B. (1963) Aspects of calcification in planktonic foraminifera (Sarcodina). *Annals of New York Academy of Sciences* **109**, 65.

Bé A.W.H., Hemleben C., Anderson O.R. and Spindler M. (1979) Chamber Formation in Planktonic Foraminifera. *Micropaleontology* **25**, 294-307.

Butler M.F., Glaser N., Weaver A.C., Kirkland M. and Heppenstall-Butler M. (2006) Calcium Carbonate Crystallization in the Presence of Biopolymers. *Cryst. Growth Des.* **6**, 781-794.

Cacace M.G., Landau E.M. and Ramsden J.J. (1997) The Hofmeister series: salt and solvent effects on interfacial phenomena. *Q. Rev. Biophys.* **30**, 241-277.

Chevalier N.R. (2014) Do Surface Wetting Properties Affect Calcium Carbonate Heterogeneous Nucleation and Adhesion? *The Journal of Physical Chemistry C* **118**, 17600-17607.

Crenshaw M.A. (1972) The inorganic composition of molluscan extrapallial fluid. *The Biological Bulletin* **143**, 506.

de Kerchove A.J. and Elimelech M. (2006) Structural Growth and Viscoelastic Properties of Adsorbed Alginate Layers in Monovalent and Divalent Salts. *Macromolecules* **39**, 6558-6564.

De Yoreo J.J. and Vekilov P.G. (2003) Principles of Crystal Nucleation and Growth. *Rev. Mineral. Geochem.* **54**, 57-93.

De Yoreo J.J., Waychunas G.A., Jun Y.-S. and Fernandez-Martinez A. (2013) In situ Investigations of Carbonate Nucleation on Mineral and Organic Surfaces. *Rev. Mineral. Geochem.* **77**, 229-257.

Frank B.P. and Belfort G. (2003) Polysaccharides and sticky membrane surfaces: critical ionic effects. *J. Membr. Sci.* **212**, 205-212.

Giuffre A.J., Hamm L.M., Han N., De Yoreo J.J. and Dove P.M. (2013) Polysaccharide chemistry regulates kinetics of calcite nucleation through competition of interfacial energies. *Proc. Natl. Acad. Sci.* **110**, 9261-9266.

Hamm L.M., Giuffre A.J., Han N., Tao J., Wang D., De Yoreo J.J. and Dove P.M. (2014) Reconciling disparate views of template-directed nucleation through measurement of calcite nucleation kinetics and binding energies. *Proc. Natl. Acad. Sci.* **111**, 1304-1309.

Hemleben C.H., Erson O.R., Berthold W. and Spindler M. (1986) *Calcification and chamber formation in Foraminifera - A brief overview*. Clarendon Press, Oxford.

Hu Q., Nielsen M.H., Freeman C.L., Hamm L.M., Tao J., Lee J.R.I., Han T.Y.J., Becker U., Harding J.H., Dove P.M. and Yoreo J.J.D. (2012) The thermodynamics of calcite nucleation: Classical vs. Non-classical pathways. *Faraday Discuss.* **159**, 509-523.

Knoll A.H. (2003) Biomineralization and evolutionary history (in Biomineralization). *Rev. Mineral. Geochem.* **54**.

Leak L.V. (1967) Fine structure of the mucilaginous sheath of Anabaena sp. *Journal of Ultrastructure Research* **21**, 61-74.

Li Q., Fernandez-Martinez A., Lee B., Waychunas G.A. and Jun Y.-S. (2014) Interfacial Energies for Heterogeneous Nucleation of Calcium Carbonate on Mica and Quartz. *Environ. Sci. Technol.*

Lowenstam H.A. and Weiner S. (1989) *On biomineralization*. Oxford University Press New York.

Manning G.S. (1969) Limiting laws and counterion condensation in polyelectrolyte solutions I. Colligative properties. *The journal of chemical Physics* **51**, 924-933.

Manoli F. and Dalas E. (2000) Spontaneous precipitation of calcium carbonate in the presence of chondroitin sulfate. *J. Cryst. Growth* **217**, 416-421.

Manoli F. and Dalas E. (2002) The effect of sodium alginate on the crystal growth of calcium carbonate. *J. Mater. Sci.: Mater. Med.* **13**, 155-158.

Manoli F., Koutsopoulos S. and Dalas E. (1997) Crystallization of calcite on chitin. *J. Cryst. Growth* **182**, 116-124.

Nielsen J.W., Sand K.K., Pedersen C.S., Lakshtanov L.Z., Winther J.R., Willemoës M. and Stipp S.L.S. (2012) Polysaccharide Effects on Calcite Growth: The Influence of Composition and Branching. *Cryst. Growth Des.* **12**, 4906-4910.

Rao A., Berg J.K., Kellermeier M. and Gebauer D. (2014) Sweet on biomineralization: effects of carbohydrates on the early stages of calcium carbonate crystallization. *Eur. J. Mineral.*

Rudall K.M. (1963) The Chitin/Protein Complexes of Insect Cuticles. In *Advances in Insect Physiology* (eds. J.E.T. J.W.L. Beament and V.B. Wigglesworth). Academic Press, London. pp. 257-313.

Sand K.K., Pedersen C.S., Sjöberg S., Nielsen J.W., Makovicky E. and Stipp S.L.S. (2014) Biomineralization: Long-Term Effectiveness of Polysaccharides on the Growth and Dissolution of Calcite. *Cryst. Growth Des.*

Weiner S. and Addadi L. (2011) Crystallization pathways in biomineralization. *Annu. Rev. Mater. Res.* **41**, 21-40.

Weiss I.M. and Schönitzer V. (2006) The distribution of chitin in larval shells of the bivalve mollusk Mytilus galloprovincialis. *J. Struct. Biol.* **153**, 264-277.

Xu L.-C., Vadillo-Rodriguez V. and Logan B.E. (2005) Residence time, loading force, pH, and ionic strength affect adhesion forces between colloids and biopolymer-coated surfaces. *Langmuir* **21**, 7491-7500.

CHAPTER 2. POLYSACCHARIDE CHEMISTRY REGULATES KINETICS OF CALCITE NUCLEATION THROUGH COMPETITION OF INTERFACIAL ENERGIES

Giuffre, A.J.; Hamm, L.M.; Han, N.; De Yoreo, J.J.; and P.M. Dove (2013) *Proceedings for the National Academy of Science* **110**:9261-9266.

2.1. ABSTRACT

Calcified skeletons are produced within complex assemblages of proteins and polysaccharides whose roles in mineralization are not well understood. Here we quantify the kinetics of calcite nucleation onto a suite of high-purity polysaccharide (PS) substrates under controlled conditions. The energy barriers to nucleation are PS-specific by a systematic relationship to PS charge density and substrate structure that is rooted in minimization of the competing substrate–crystal and substrate–liquid interfacial energies. Chitosan presents a low-energy barrier to nucleation because its near-neutral charge favors formation of a substrate–crystal interface, thus reducing substrate interactions with water. Progressively higher barriers are measured for negatively charged alginates and heparin that favor contact with the solution over the formation of new substrate–crystal interfaces. The findings support a directing role for PS in biomineral formation and demonstrate that substrate–crystal interactions are one end-member in a larger continuum of competing forces that regulate heterogeneous crystal nucleation.

2.2. INTRODUCTION

Efforts to decipher patterns of biomineralization have identified proteins and PS as major components of the organic matrices associated with sites of calcification. In mollusks and other organisms that include the red algae, coccolithophores, and foraminifera (Simkiss, 1965; Weiner and Traub, 1980; **Table 2.1**), calcifying macromolecules are dominated by functional groups with an acidic character— proteins that are rich in carboxylated amino acids (Weiner et al., 1975) and PS that are highly sulfated and carboxylated (Crenshaw et al., 1976; Wada, 1980). Although a physical picture of these interactions is not well developed, this recurring affiliation of carboxylate and sulfate groups with zones of mineralization in organisms suggests specific roles for macromolecules in nucleation and growth. Early studies have led the biomineralization community to generally assume that charged proteins actively regulate mineralization. In contrast, PS, such as the chitin found in the insoluble fraction of the mollusk shell, are thought to provide an inert scaffolding to support these proteins (Rudall, 1963; Weiss et al., 2006).

Recent studies challenge this assumption with qualitative evidence that PS can also promote calcium carbonate ($CaCO_3$) mineralization (Furuhashi et al., 2009; Ehrlich, 2010; **Table 2.1**). For example, specific orientations of chitin fibers with neutral functional groups promote the templating of $CaCO_3$ in the lobster carapace (Giraud-Guille et al., 2004; Al-Sawalmih et al., 2008), crab cuticle (Giraud-Guille et al., 2004), and nautilus shell (Nudelman et al., 2006). More generally, the monosaccharide sequences along PS chains can influence biological function and their interactions with

proteins (Björk et al., 1982). This suggests PS chemistry and interactions with proteins could regulate patterns of mineralization.

Table 2.1: Examples of polysaccharides found at sites of $CaCO_3$ mineralization from diverse phyla.

Name	Structure	Polysaccharide	Ref.
Red algae (Rhodophyta)			
Corallina pilulifera (P. *et* R.)	Cell wall of thallus	Xylogalactan*, sulfated, methylated, agaran-like Floridean starch Alginic acid	(Usov et al., 1995; Usov et al., 1997)
Joculator maximus (Manza)	Cell wall of thallus	Xylogalactan*, sulfated, methylated	(Takano et al., 1996)
Coccolithophores (Haptophyta)			
Emiliania huxleyi	Coccolith	Mannan*, sulfated, branched with uronic acids and methylated sugars	(Fichtinger-Schepman et al., 1980; de Vrind-de Jong et al., 1986)
Pleurochrysis carterae	Coccolith	Galacturonan*, sulfated, other uronic acids Glucuronan* with tartarate and glyoxylate residues	(de Vrind-de Jong et al., 1986; Marsh et al., 1992)
Cyanobacteria (Cyanophyta)			
Anabaena sp.	Mucilaginous sheath	Pectin Glycosaminoglycan†	(Leak, 1967)
Foraminifera (Foraminifera)			
Heterostegina depressa	Test	Glycosaminoglycan†, sulfated	(Weiner et al., 1984)
Mollusks (Mollusca)			
Nautilus repertus	Nacreous shell layer	β-Chitin	(Weiner et al., 1980)
Mercenaria mercenaria	Extrapallial fluid	Glycosaminoglycan†, sulfated	(Crenshaw, 1972)
Insects (Arthropoda)			
Carcinus maenus (L.)	Cuticle	α-Chitin	(Giraud-Guille, 1984)
Homarus americanus	Carapace	α-Chitin	(Al-Sawalmih et al., 2008)

* See references for more detail on structure and sequence.
† Glycosaminoglycan is a broad classification with ambiguous chemical structure.

Anecdotal observations from *in vitro* studies also support the thinking that PS influence mineral formation but their specific effects are unclear. For example, PS with higher carboxyl and sulfate content promote either faster (Borman et al., 1987; Arias et al., 2002) or slower (Borman et al., 1982; Butler et al., 2006) rates of $CaCO_3$ nucleation. While these results appear inconsistent at first glance, the differences are likely attributable to the diverse experimental designs that were used across disciplines and, in some cases, with little control on chemical conditions. Though qualitative, insights from *in vivo* and *in vitro* studies provide evidence that the chemical structure of PS can indeed control calcite nucleation. They also raise the question of whether there is an underlying

relationship between homologies of mineralization and the functional group chemistry of monosaccharide sequences, and more generally, the chemistry and structure of macromolecules.

To test this idea, we designed an experimental study to quantify the underlying energetic controls on calcite nucleation. A suite of high purity PS with regular monomer sequences and simple functional group chemistry were chosen as model compounds for the complex PS found in calcifying organisms (**Fig. 2.1**). Heparin is the most highly charged PS of the group with carboxyl and sulfate groups while amine groups give chitosan a small net positive charge. Two alginates provided a test of how stereochemistry influences nucleation through different proportions of the stereoisomers mannuronic and guluronic acid.

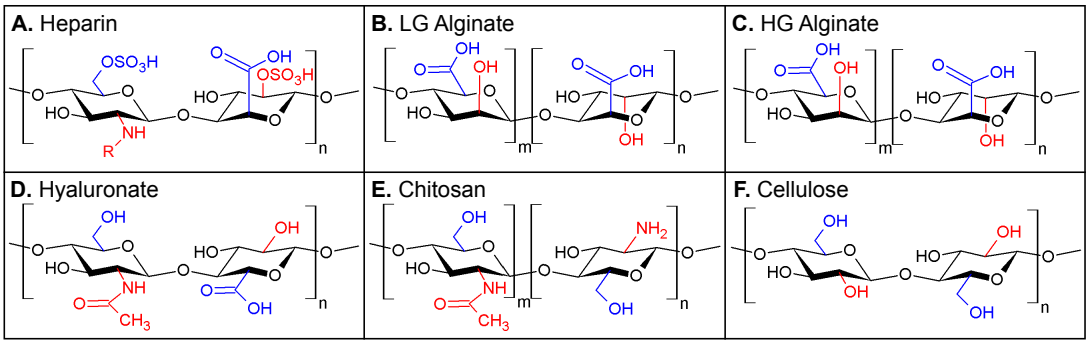

Fig. 2.1: Polysaccharide chemical structures illustrate the functional groups attached to 2-carbon (red) and 6-carbon (blue) of each ring. (**A**) De-N-sulfated Heparin contains amine, acetylamine, carboxyl, and sulfate groups. R is 80% H and 20% $COCH_3$. 90% of carboxyl groups are in axial position. (**B and C**) Alginates contain carboxyl groups with different proportions of guluronic acid monomer content. (**D**) Hyaluronate contains acetylamine and carboxyl groups. (**E**) Chitosan contains amine and acetylamine groups. (**F**) Cellulose, with only hydroxyl groups, was not used in study and is included for comparison.

Using a flow-through method that controlled for solution chemistry (Hu et al., 2012), we quantified the number of crystallites that formed on each type of PS substrate. These were prepared by electrodeposition onto gold using established methods. Rate

measurements assumed that each nucleus that achieved a critical radius subsequently continued to grow into an observable crystallite. The number of crystals per mm^2 was counted in a sequence of time-lapsed images to determine nucleation rates (**insets of Fig. 2.2ABCD**) across a series of solution supersaturations, σ, defined by:

$$\sigma = \ln \frac{a_{Ca^{2+}} a_{CO_3^{2-}}}{K_{sp}} \qquad [2.1]$$

where a_i is the activity of species i and K_{sp} is the equilibrium solubility constant ($10^{-8.48}$ for pure calcite at 25°C). The σ varied from 4.83 - 5.63 (**Table B3**) at a constant solution pH of 10.8±0.1, a_{Ca}/a_{CO3} of 1.0, temperature of 25.0±0.5°C, and total ionic strength of 7.6 to 13.0 mM. Despite the high supersaturations that exceeded the solubility of amorphous calcium carbonate, we identified only calcite crystallites according to their rhombohedral morphologies under these conditions, consistent with previous work (Butler et al., 2006).

2.3. MATERIALS AND METHODS

2.3.1. Preparation of PS films

PS substrates were deposited onto gold-coated Si wafers (Platypus) using established electrodepostion protocols (Wu et al., 2002; Zhitomirsky, 2002; Cheong et al., 2008; Ma et al., 2010). The electrodeposition apparatus consisted of two ~1.5 cm^2 wafers that were held 15 mm apart by a Teflon spacer and connected to an electrophoresis power supply using stainless steel alligator clips. For each type of film, the electrodes were submerged in 0.05% solutions of LG sodium alginate (<50% guluronic acid, Novamatrix), HG sodium alginate (>75% guluronic acid, Novamatrix), sodium hyaluronate (Novamatrix), chitosan chloride (75-90% deacetylated, Novamatrix) and de-N-sulfated heparin (20% N-acetylated, Sigma Aldrich), prepared at room temperature by gently mixing into 18.2MΩ·cm ultrapure water for 1 hour. The film was

deposited by applying a 20 V current for 15-25 minutes. The integrity of PS film was confirmed before and after crystallization by SEM imaging or Alcian Blue (Sigma Aldrich) staining of carboxylated polysaccharides.

2.3.2. Measurement of nucleation rates

Rates of heterogeneous calcite nucleation were measured using a flow-through method that maintained controlled supersaturation conditions for the duration of each experiment. Experiments began by placing a freshly prepared substrate inside an acrylic glass flow chamber and sealed with a glass coverslip. Solutions of 3 to 7 mM $CaCl_2 \cdot 2H_2O$ (≥99% Sigma Aldrich) and Na_2CO_3 (99.997% Alfa Aesar) were prepared and placed in two polypropylene syringes that were connected to the flow chamber with Tygon tubing and a T junction. The syringes were loaded onto a high precision syringe pump (Harvard Apparatus, PHD 2000 Infusion) and dispensed at a constant flow rate of 30 mL/hr. Prior to each crystallization experiment, the substrate, flow chamber system and tubing were flushed with distilled deionized water. The experiments were conducted at a suite of solution supersaturations, σ, ranging from 4.83 to 5.63, but were held at constant pH of 10.8±0.1, constant a_{Ca}/a_{CO3} of 1, and constant temperature of 25.0±0.5°C. The short residence time of solution in the flow chamber allowed us to assume that solution pH and σ remained constant for the entire experiment.

Each experiment proceeded by collecting time lapse images of crystallites that formed onto the substrates as a series of time-lapse images under an optical microscope at 10x magnification. Rates of nucleation were determined using only data within steady state nucleation conditions. We assumed all nuclei that achieve a critical size grow into

an observable crystallite. The maximum duration of an individual experiment was 1 hour; upon which time the substrate was removed and rinsed with ethanol.

2.3.3. Measurements of surface free energy

The $\gamma_{S\text{-}air}$ measurements were conducted using a well-established method by Owens, Wendt, Rabel, and Kaelble (Owens et al., 1969; Kaelble, 1970; Rabel, 1971). Static contact angle, θ, was measured with a goniometer on electrodeposited PS substrates using three test liquids: 18.2MΩ·cm ultrapure water, glycerol (Fisher, 99.5%), and ethylene glycol (Aldrich, 99.7%) with known polar and dispersive components to surface free energy (γ_L^p and γ_L^d). Six angle measurements (three left and three right) were made on three replicate droplets of each test liquid (See **Appendix B1** for details).

2.4. RESULTS AND DISCUSSION

The number of calcite crystallites that nucleated and grew on the PS substrates was proportional to the driving force, σ, of the reactant solution (**insets** of **Fig. 2.2 ABCD**). Rates were also PS-specific with the highest and lowest number densities measured for heparin and chitosan, respectively (**Fig. 2.2A, 2.2D**).

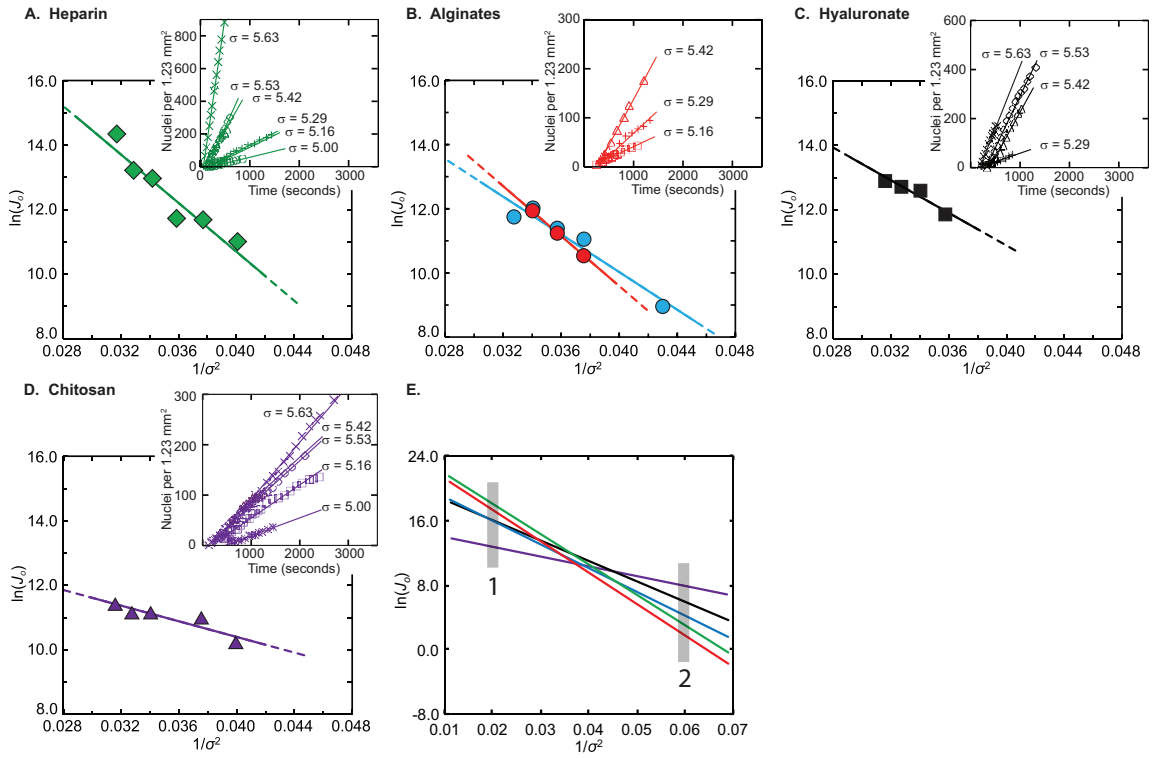

Fig. 2.2: Calcite steady-state nucleation rates obey classical nucleation theory (Eq. 2.2) and show PS-specific dependence on B, a proxy for the thermodynamic barrier to nucleation. Data are quantified from slopes of experimental rate data shown in insets. (**A**) Heparin, $B = 376 \pm 60$; (**B**) LG alginate (red circles), $B = 390 \pm 11$ and HG alginate (blue circles), $B = 294 \pm 45$; (**C**) Hyaluronate, $B = 253 \pm 58$; and (**D**) Chitosan, $B = 121 \pm 22$. Standard errors of $\ln(J_o)$ are smaller than the diameter of symbols. (**E**) Trends in **A-D** extrapolated to (1) large and (2) small supersaturations predicts reversal in relative order of nucleation rates.

To quantify the thermodynamic basis for these differences, we evaluated the linear portion of the nuclei versus time data using classical nucleation theory (Nielsen, 1964; Chernov, 1984; **Appendix B2**). The linear form of the general nucleation expression states that the flux of new nuclei onto a substrate is described by:

$$\ln(J_o) = \ln(A) - \frac{B}{\sigma^2} \qquad [2.2]$$

where J_o is the steady state rate of heterogeneous nucleation (m^{-2} s^{-1}); A is dependent upon kinetic factors that include rates of ion desolvation, attachment, and detachment; and slope, B, is given by

$$B = \frac{F\omega^2\gamma_{net}^3}{k_B^3 T^3} \qquad [2.3]$$

where F is a nucleus shape factor, ω is the molecular volume of calcite, k_B is the Boltzmann constant, T is temperature, and γ_{net} is the net surface free energy of the crystal-substrate-liquid system (mJ m^{-2}). Assuming that ω is relatively constant, the experimental variable within B is γ_{net} for a constant T. Because B is a proxy for the thermodynamic barrier to the nucleation (**Appendix B2**), its dependence upon γ_{net} represents the contribution of surface energies to the energy barrier. **Eq. (2.2)** gives a good fit to the rate data and shows that at the highest supersaturations, substrates rich with carboxyl and sulfate functional groups (**Fig. 2.2ABC**) promote the fastest nucleation rates while the slowest rates occur on chitosan surfaces (**Fig 2.2D**).

By evaluating the slopes of these trends, we find that values of B are PS-specific. The highest slopes, and thus, the highest energy barriers to nucleation are correlated with the charge-dense substrates (LG alginate and heparin). In contrast, nucleation onto chitosan substrates shows the lowest slope. Because B is directly proportional to surface energy cubed (**Eq. 2.3**), we can deduce that a low value of B is correlated with a low net surface energy. Our estimate of a low γ_{net} for chitosan is consistent with the surface energy values reported in a previous nucleation study (Manoli et al., 1997). Comparisons of the two alginates show the HG form (high guluronic acid content) has a smaller thermodynamic barrier to nucleation than LG alginate.

To decipher the physical basis for nucleation barriers estimated for each PS, we first examine the dependence of B on net charge. The expected charge per monosaccharide is estimated using reported acid dissociation constants of the functional groups for each PS and chemical characterizations by the vendor (**Appendix B3**). For

our experimental conditions (final pH of the mixed solutions = 10.8±0.1), carboxyl and sulfate functional groups are negatively charged whereas hydroxyl, acetylamine, and amine groups have a neutral or slightly positive net charge. Polysaccharides with mixed functional group chemistry are assigned an average charge.

By correlating the average monosaccharide charge of each PS with *B*, we find a direct relationship (**Fig. 2.3A**). Heparin and the alginates, which derive a higher negative charge from carboxyl groups, are correlated with greater *B* values and, therefore, greater thermodynamic barriers to nucleation (**Fig. 2.3A**). In contrast, the small net positive charge of chitosan is associated with the lowest energy barrier to nucleation. The relationship in **Fig. 2.3A** suggests net charge of a PS influences nucleation through the surface free energy of the substrate-liquid-crystal system.

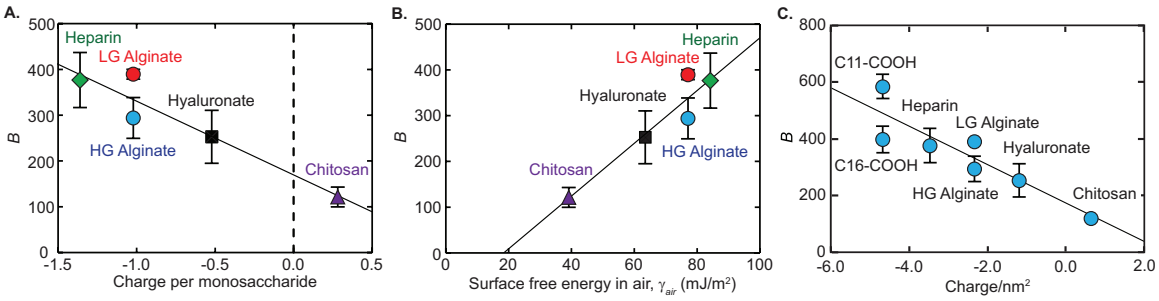

Fig. 2.3: Kinetic measurements provide insights to controls on thermodynamic barriers to nucleation. (**A**) Barriers are inversely correlated with charge density such that near-neutral PS present the lowest barrier to calcite formation. (**B**) Measurements of surface free energy in air, a proxy for γ_{SL}, provide evidence for a competition between solvent and crystal interactions with the PS that correlate with hydrophilicity. (**C**) Relationship between energy barrier and charge density can also explain the very high energy barrier measured on carboxylated SAMs. Offsets between SAMs and alginates of different chain lengths and stereochemistry suggest functional group structure and conformation also tune barrier height. Standard errors of *B* are derived from the linear fits of **Eq. (2.2)** to data in **Fig. 2.2**.

We can relate the observed trend to the underlying crystal- and solution-substrate interactions by evaluating the factors that influence the value of γ_{net} contained in *B*. Recall that the net surface free energy, γ_{net}, is a composite of three contributions:

$$\gamma_{net} = \gamma_{LC} + h(\gamma_{SC} - \gamma_{SL}) \qquad [2.4]$$

where γ_{ij} is the interfacial free energy of the liquid-crystal (LC), substrate-crystal (SC), and substrate-liquid (SL) interface, and h is a nucleus shape factor (for example, h = ½ for a hemisphere.) For the conditions of these experiments, we assume that γ_{LC} is approximately constant. Thus, the higher values of B that we estimate for nucleation onto the most negatively charged PS are associated with large γ_{SC}, small γ_{SL} or some combination of the two.

In principle, one can test the hypothesis that large negative charge is the basis for the large barrier to nucleation via smaller substrate-liquid energies by conducting independent measurements of γ_{SL} for each of the PS substrates. Unfortunately, this quantity is difficult to measure. Instead, we measured $\gamma_{S\text{-}air}$ using established methods (Owens et al., 1969; Rabel, 1971; Kaelble, 1970; **Fig. B1**, **Appendix B1**) to serve as a rough proxy for γ_{SL}. This value also provides insight on the hydrophilicity of the substrates. That is, surfaces with a large amount of charge prefer interaction with polar water molecules and therefore exhibit greater surface free energies while exposed to air and smaller surface free energies in water. Recall that smaller γ_{SL}, which corresponds to larger $\gamma_{S\text{-}air}$, contributes to a greater γ_{net} (**Eq. (2.4)**) and thus a higher thermodynamic barrier to nucleation. Indeed we find PS substrates with high measured values of $\gamma_{S\text{-}air}$ correlate with greater thermodynamic barriers to nucleation (**Fig. 2.3B**).

The trends in **Fig. 2.3A** and **2.3B** thus suggest the possibility of a broader relationship that could explain calcite nucleation behavior onto substrates ranging from neutral to highly charged. Measurements of energetic barriers to calcite nucleation onto carboxylated self-assembled monolayers provide insights into the influence of highly

charged functional groups that are found in proteins and PS in mineralizing systems (Hu et al., 2012). Due to the greater hydrophilicity of these substrates, the method of measuring $\gamma_{S\text{-}air}$ cannot be used because the contact angles lie outside of the accessible range. Instead we estimate the surface charge density from pK_a values of functional groups and packing density of the SAMs or PS (**Appendix B3**). **Fig. 2.3C** shows that, indeed, charge density is correlated with the barrier height to calcite nucleation along a single trend that includes the SAM substrates.

The implication of **Fig. 2.3C** is that charge density through functional group chemistry has a primary control on the barrier to nucleation through differences in γ_{SL}. Small offsets in B between the two alginates and the carboxylated SAMs (**Fig. 2.3C**) suggest that differences in the structure of substrates with similar charge densities further regulate the barrier height. This conclusion is supported by recent simulations showing that variations in head group geometry that arise from SAM-monomer interactions cause subtle differences in substrate-crystal interfacial energies (Nielsen et al., 2012). Thus nucleation barriers are largely controlled by substrate charge density through γ_{SL} and further regulated by small differences in γ_{SC} through subtle variations in structure.

Our results demonstrate the energy barrier to calcite nucleation is determined by a competition between the energetics of crystal nucleus attachment to a substrate and creating new interface (γ_{SC}) versus the energetics of eliminating a solvated substrate (γ_{SL}). By minimizing the change in free energy through these thermodynamic drivers, the systematic relationship between nucleation and the chemistry and structure of substrate environments can be understood. Hydrophilic substrates prefer to maintain the substrate-water interface, thus presenting a high barrier to making a new substrate-crystal interface.

In contrast, neutral to less hydrophilic surfaces present a lower thermodynamic barrier to displacing water to form a new substrate-crystal interface and thus, to mineral nucleation. This interpretation of the experimental data expands upon the conclusions of earlier computational studies that explored the importance of surface ionization, as well as the competition between the energies of the substrate-crystal and liquid-crystal interfaces (Duffy et al., 2004).

At first glance, the higher energy barriers we estimate for nucleation onto charged surfaces are counterintuitive given the long-standing perception that negatively charged functional groups *promote* nucleation by strong interactions with Ca^{2+} ions (Weiner et al., 1975; Crenshaw et al., 1976; Addadi et al., 1987; Suzuki et al., 2009). Moreover, a number of studies observe that calcite crystallites are preferentially formed on carboxyl-patterned regions in sharp contrast to the surrounding hydrophobic methyl-functionalized areas (Aizenberg et al., 1999; Hosada et al., 2001; Kim et al., 2007).

To understand why these seemingly disparate observations are consistent, recall that energy barriers are constant for a given substrate-liquid-crystal system and nucleation rates are dependent upon σ^{-2}. Thus for any two substrates, there must be a value of σ above which, paradoxically, the one with the higher value of B gives *faster* nucleation rates (**Fig. 2.2E**). Because the studies described above were conducted at extremely high levels of supersaturation, the charge-dense macromolecules produced the most crystallites over short time intervals. **Fig 2.2E** shows that as supersaturation is lowered, these trends eventually flip and neutral substrates with lower energy barriers promote the fastest rates of nucleation (**Eq. 2.2**). This physical picture reiterates the point that while energy barriers to nucleation at a given supersaturation are constant and

substrate-specific, the local supersaturation environment has the overarching control on relative rates of nucleation onto charged versus neutral substrates.

The findings suggest a simple mechanism-based framework for understanding nucleation as a continuum of substrate-liquid-crystal interactions that are governed by acidic and neutral chemical domains, irrespective of macromolecular class. The possibility of regulating the onset of nucleation by this construct suggests the need to revisit the long-standing assumptions regarding the roles of neutral and acidic macromolecules at sites of calcification. If neutral macromolecules present a lower energy barrier to nucleation by promoting the formation of new substrate-crystal interfaces, an important part of the mineralization picture may be currently missing.

2.5. IMPLICATIONS

There are a number of implications for interpreting the origins of biominerals that form in organisms and for better controls on materials synthesis. By establishing a physical basis for how macromolecule chemistry favors or inhibits biomineral nucleation, it may be possible to interpret patterns of skeletal biomineralization through geologic time using an inverse approach. That is, differential expression of PS and proteins with varying charge density, in concert with local supersaturation, regulate the placement, timing and extent of mineral nucleation. For example, modern mollusks induce mineralization at epithelial membranes within neutral chitin matrices using acidic proteins, hydrophobic silk proteins, and glycosaminoglycans in the growth front of the shell (Marxen et al., 1998; Addadi et al., 2006; Kim et al., 2007; Furuhashi et al., 2009). Recall that the chitin and glycosaminoglycans found in organisms are, in fact, glycoproteins (Rudall, 1963; Langer, 1992; Weiss et al., 2006).

These results also cast a new light on the processes of crystal templating and epitaxy. Heterogeneous nucleation theory has long-recognized the contributions of interfacial energies as the primary drivers to minimizing the overall energy of the system (Volmer et al., 1926). However, conventional wisdom focused on epitaxy mechanisms and assumed that substrate-crystal interactions were predominant in nucleating environments (Turnbull et al., 1952; Chernov, 1984). Our findings show this assumption must now be reconsidered within a broader mechanistic framework whereby the drivers to nucleation are a continuum of substrate-liquid-crystal interactions. This explains why the basic tenets of classical nucleation theory have always allowed for the possibility that poor substrate-crystal interfaces can promote nucleation. We show this can occur by eliminating a less favorable substrate-liquid interface. By considering nucleation as a continuum of interactions, a new paradigm for understanding diverse nucleation phenomena may emerge.

2.6. REFERENCES

Addadi L., Joester D., Nudelman F. and Weiner S. (2006) Mollusk Shell Formation: A Source of New Concepts for Understanding Biomineralization Processes. *Chem.-Eur. J.* **12**, 980-987.

Addadi L., Moradian J., Shay E., Maroudas N.G. and Weiner S. (1987) A chemical model for the cooperation of sulfates and carboxylates in calcite crystal nucleation: relevance to biomineralization. *Proc. Natl. Acad. Sci.* **84**, 2732-2736.

Aizenberg J., Black A.J. and Whitesides G.M. (1999) Control of crystal nucleation by patterned self-assembled monolayers. *Nature* **398**, 495-498.

Al-Sawalmih A., Li C., Siegel S., Fabritius H., Yi S., Raabe D., Fratzl P. and Paris O. (2008) Microtexture and Chitin/Calcite Orientation Relationship in the Mineralized Exoskeleton of the American Lobster. *Adv. Funct. Mater.* **18**, 3307-3314.

Arias J.I., Jure C., Wiff J.P., Fernández M.S., Fuenzalida V. and Arias J.L. (2002) Effect of sulfate content of biomacromolecules on the crystallization of calcium carbonate. *Mater. Res. Soc. Symp. Proc.* **711**, HH1.7.1-HH1.7.6.

Björk I. and Lindahl U. (1982) Mechanism of the anticoagulant action of heparin. *Mol. Cell. Biochem.* **48**, 161-182.

Borman A.H., de Jong E.W., Huizing M., Kok D.J., Westbroek P. and Bosch L. (1982) The Role in CaCO3 Crystallization of an Acid Ca2+-Binding Polysaccharide Associated with Coccoliths of Emiliania huxleyi. *Eur. J. Biochem.* **129**, 179-183.

Borman A.H., de Jong E.W., Thierry R., Westbroek P., Bosch L., Gruter M. and Kamerling J.P. (1987) Coccolith-associated polysaccharides from cells of Emiliania huxleyi (Haptophyceae). *Journal of Phycology* **23**, 118-123.

Butler M.F., Glaser N., Weaver A.C., Kirkland M. and Heppenstall-Butler M. (2006) Calcium Carbonate Crystallization in the Presence of Biopolymers. *Cryst. Growth Des.* **6**, 781-794.

Cheong M. and Zhitomirsky I. (2008) Electrodeposition of alginic acid and composite films. *Colloids and Surfaces A: Physicochemical and Engineering Aspects* **328**, 73-78.

Chernov A.A. (1984) *Modern Crystallography III - Crystal Growth*. Springer-Verlag, Berlin.

Crenshaw M.A. (1972) The inorganic composition of molluscan extrapallial fluid. *The Biological Bulletin* **143**, 506.

Crenshaw M.A. and Ristedt H. (1976) The histochemical localization of reactive groups in septal nacre from Nautilus pompilius L. In *The Mechanisms of Mineralization in the Invertebrates and Plants* (eds. N. Watabe and K.M. Wilbur). University of South Carolina Press, Columbia, South Carolina. pp. 355-367.

de Vrind-de Jong E.W., Borman A.H., Thierry R., Westbroek P., Gruter M. and Kamerling J.P. (1986) Calcification in the coccolithophorids Emiliania huxleyi and Pleurochrysis carterae II. Biochemical aspects. In *Biomineralization in Lower Plants and Animals* (eds. B.S.C. Leadbeater and R. Riding). Oxford University Press, Oxford, New York. pp. 205-217.

Duffy D.M. and Harding J.H. (2004) Simulation of Organic Monolayers as Templates for the Nucleation of Calcite Crystals. *Langmuir* **20**, 7630-7636.
Ehrlich H. (2010) Chitin and collagen as universal and alternative templates in biomineralization. *International Geology Review* **52**, 661-699.
Fichtinger-Schepman A.M.J., Kamerling J.P., Versluis C. and Vliegenthart J.F.G. (1980) Structural analysis of acidic oligosaccharides derived from the methylated, acidic polysaccharide associated with coccoliths of Emiliania huxleyi (lohmann) kamptner. *Carbohydr. Res.* **86**, 215-225.
Furuhashi T., Schwarzinger C., Miksik I., Smrz M. and Beran A. (2009) Molluscan shell evolution with review of shell calcification hypothesis. *Comparative Biochemistry and Physiology, Part B* **154**, 351-371.
Giraud-Guille M.-M. (1984) Fine structure of the chitin-protein system in the crab cuticle. *Tissue and Cell* **16**, 75-92.
Giraud-Guille M.-M., Belamie E. and Mosser G. (2004) Organic and mineral networks in carapaces, bones and biomimetic materials. *C. R. Palevol* **3**, 503-513.
Hosada N. and Kato T. (2001) Thin-film formation of calcium carbonate crystals: effects of functional groups of matrix polymers. *Chem. Mater.* **13**, 688-693.
Hu Q., Nielsen M.H., Freeman C.L., Hamm L.M., Tao J., Lee J.R.I., Han T.Y.J., Becker U., Harding J.H., Dove P.M. and Yoreo J.J.D. (2012) The thermodynamics of calcite nucleation: Classical vs. Non-classical pathways. *Faraday Discuss.* **159**, 509-523.
Kaelble D.H. (1970) Dispersion-polar surface tension properties of organic solids. *The Journal of Adhesion* **2**, 66-81.
Kim Y.-Y., Douglas E.P. and Gower L.B. (2007) Patterning Inorganic (CaCO3) Thin Films via a Polymer-Induced Liquid-Precursor Process. *Langmuir* **23**, 4862-4870.
Langer M.R. (1992) Biosynthesis of glycosaminoglycans in foraminifera: A review. *Marine Micropaleontology* **19**, 245-255.
Leak L.V. (1967) Fine structure of the mucilaginous sheath of Anabaena sp. *Journal of Ultrastructure Research* **21**, 61-74.
Ma R., Epand R.F. and Zhitomirsky I. (2010) Electrodeposition of hyaluronic acid and huyaluronic acid-bovine serum albumin films from aqueous solutions. *Colloids and Surfaces B: Biointerfaces* **77**, 279-285.
Manoli F., Koutsopoulos S. and Dalas E. (1997) Crystallization of calcite on chitin. *J. Cryst. Growth* **182**, 116-124.
Marsh M.E., Chang D.-K. and King G.C. (1992) Isolation and characterization of a novel acidic polysaccharide containing tartarate and glyoxylate residues from the mineralized scales of a unicellular coccolithophorid alga Pleurochrysis carterae. *J. Biol. Chem.* **267**, 20507-20512.
Marxen J.C., Hammer M., Gehrke T. and Becker W. (1998) Carbohydrates of the Organic Shell Matrix and the Shell-Forming Tissue of the Snail Biomphalaria glabrata (Say). *Biological Bulletin* **194**, 231-240.
Nielsen A.E. (1964) *Kinetics of Precipitation*. Pergamon Press Limited, Oxford.
Nielsen M.H., Lee J.R.I., Hu Q., Yong-Jin Han T. and De Yoreo J.J. (2012) Structural evolution, formation pathways and energetic controls during template-directed nucleation of CaCO3. *Faraday Discuss.* **159**, 105-121.

Nudelman F., Gotliv B.A., Addadi L. and Weiner S. (2006) Mollusk shell formation: Mapping the distribution of organic matrix components underlying a single aragonitic tablet in nacre. *J. Struct. Biol.* **153**, 176-187.

Owens D.K. and Wendt R.C. (1969) Estimation of the surface free energy of polymers. *J. Appl. Polym. Sci.* **13**, 1741-1747.

Rabel W. (1971) Einige Aspekte der Benetzungstheorie und ihre Anwendung auf die Untersuchung und Veränderung der Oberflächeneigenschaften von Polymeren. *Farbe und Lack* **77**, 997-1006.

Rudall K.M. (1963) The Chitin/Protein Complexes of Insect Cuticles. In *Advances in Insect Physiology* (eds. J.E.T. J.W.L. Beament and V.B. Wigglesworth). Academic Press, London. pp. 257-313.

Simkiss K. (1965) The organic matrix of the oyster shell. *Comparative Biochemistry and Physiology* **16**, 427-435.

Suzuki M., Saruwatari K., Kogure T., Yamamoto Y., Nishimura T., Kato T. and Nagasawa H. (2009) An Acidic Matrix Protein, Pif, Is a Key Macromolecule for Nacre Formation. *Science* **325**, 1388-1390.

Takano R., Hayashi J., Hayashi K., Hara S. and Hirase S. (1996) Structure of a water-soluble polysaccharide sulfate from the red seaweed Joculator maximus Manza. *Botanica Marina* **39**, 95-102.

Turnbull D. and Vonnegut B. (1952) Nucleation Catalysis. *Industrial & Engineering Chemistry* **44**, 1292-1298.

Usov A.I., Bilan M.I. and Klochkova N.G. (1995) Polysaccharides of algae 48. Polysaccharide composition of several isolation of alginate from Corallina pilulifera P. et R. (Rhodophyta, Corallinaceae). *Botanica Marina* **38**, 43-51.

Usov A.I., Bilan M.I. and Shashkov A.S. (1997) Structure of a sulfated xylogalactan from the calcareous red alga Corallina pilulifera P. et R. (Rhodophyta, Corallinaceae). *Carbohydr. Res.* **303**, 93-102.

Volmer M. and Weber A. (1926) Keimbildung in übersättigten Gebilden. *Z. Phys. Chem. (Muenchen, Ger.)* **119**, 277-301.

Wada K. (1980) Initiation of Mineralization in Bivalve Molluscs. In *The Mechanisms of Biomineralization in Animals and Plants: Proceedings of the Third International Biomineralization Symposium* (eds. M. Omori and N. Watabe). Tokai University Press, Tokyo. pp. 79-92.

Weiner S. and Erez J. (1984) Organic Matrix of the Shell of the Foraminifer, Heterostegina depressa. *Journal of Foraminiferal Research* **14**, 206-212.

Weiner S. and Hood L. (1975) Soluble Protein of the Organic Matrix of Mollusk Shells: A Potential Template for Shell Formation. *Science* **190**, 987-989.

Weiner S. and Traub W. (1980) X-ray diffraction study of the insoluble organic matrix of mollusk shells. *FEBS Lett.* **111**, 311-316.

Weiss I.M. and Schönitzer V. (2006) The distribution of chitin in larval shells of the bivalve mollusk Mytilus galloprovincialis. *J. Struct. Biol.* **153**, 264-277.

Wu L.-Q., Gadre A.P., Yi H., Kastantin M.J., Rubloff G.W., Bentley W.E., Payne G.F. and Ghodssi R. (2002) Voltage-dependent assembly of the polysaccharide chitosan onto an electrode surface. *Langmuir* **18**, 8620-8625.

Zhitomirsky I. (2002) Cathodic electrodeposition of ceramic and organoceramic materials. Fundamental aspects. *Adv. Colloid Interface Sci.* **97**, 279-317.

CHAPTER 3: ISOTOPIC TRACER EVIDENCE FOR THE AMORPHOUS CALCIUM CARBONATE TO CALCITE TRANSFORMATION BY DISSOLUTION-REPRECIPITATION

Giuffre, A.J.; Gagnon, A.C.; De Yoreo, J.J.; and P.M. Dove. In Review for *Geochimica et Cosmochimica Acta*

3.1. ABSTRACT

Observations that some biogenic and sedimentary calcites grow from amorphous calcium carbonate (ACC) raise the question of how this mineralization process influences composition. However, the detailed pathway and geochemical consequences of the ACC to calcite transformation are poorly constrained. This experimental study investigated the formation of calcite from ACC by using magnesium and calcium stable isotope labeling to directly probe the transformation pathway and controls on composition. Four processes were considered: dissolution-reprecipitation, solid state transformation, and combinations of these end-members. To distinguish between these scenarios, ACC was synthesized from natural isotope abundance solutions and subsequently transferred to spiked solutions that were enriched in ^{43}Ca and ^{25}Mg for the transformation to calcite. Isotope measurements by NanoSIMS determined the $^{43}Ca/^{40}Ca$, and $^{25}Mg/^{24}Mg$ ratios of the resulting calcite crystals.

Analysis of the data shows the transformation is best explained by a dissolution-reprecipitation process. We find that when a small amount of ACC is transferred, the isotopic signals in the resulting calcite are largely replaced by the composition of the surrounding spiked solution. When larger amounts of ACC are transferred, calcite compositions reflect a mixture between the ACC and initial solution end-member. Comparisons of the measurements to the predictions of a simple mixing model indicate

that calcite compositions are sensitive to relative amounts of ACC and the surrounding solution reservoir and are primarily governed by the conditions at the time of ACC transformation rather than the initial ACC formation. Shifts in calcite composition over the duration of the transformation period reflect the progressive evolution of the local solution conditions. This dependence suggests the extent to which there is water available would change the end point composition on the mixing line. While these findings have significant geochemical implications, the question remains whether this transformation pathway is generally followed when biomineralization involves ACC or is particular to these inorganic experiments. Insights from this study nonetheless suggest that some types of compositional variability, such as 'vital effects', may be explained in-part by a co-evolution of reservoir and products over the duration of the transformation.

3.2. INTRODUCTION

Reports that diverse phyla accumulate reservoirs of amorphous calcium carbonate prior to mineralization (Addadi et al., 2003; Addadi et al., 2012) are motivating an extensive effort to establish a process-based understanding of calcification via this pathway. Until recently, most ACC studies have focused on the structural aspects of ACC formation and transformation. The sea urchin provides a good example of this complexity with spicule growth starting as ACC that quickly transforms to calcite. Similar pathways involving ACC have been proposed in other organisms including snails (Hasse et al., 2000), bivalves (Jacob et al., 2011), crabs (Luquet et al., 2004; Dillaman et al., 2005), lobsters (Al-Sawalmih et al., 2009), and isopods (Roer et al., 1984; Ziegler, 1994; Hild et al., 2008).

One crucial unanswered question is whether the chemical and isotopic signatures recorded in an initial ACC phase are transferred to the final calcite product. If so, this

would suggest that many carbonate biomineral-based geochemical proxies could be controlled by ACC formation and subsequent transformation. The question of when and where chemical signatures are recorded during calcification by an ACC intermediate has particular significance for efforts to reconstruct paleoenvironmental conditions from the composition and isotopic signals contained in biominerals. Such correlations provide estimates of past chemical and physical parameters such as ocean pH (Zeebe, 2005; Yu et al., 2007), temperature (Epstein et al., 1953; Emiliani, 1954; Nürnberg et al., 1996; Lea et al., 1999), redox potential (Hastings et al., 1996; Tribovillard et al., 2006), and productivity (Klein et al., 1996; Frank et al., 2000; Chase et al., 2001; Tribovillard et al., 2006).

While these environmental proxies provide remarkable insights, they are largely based upon empirical correlations between skeletal composition and environmental conditions. They also show ongoing inconsistencies that reiterate the need to establish process-based models for the signals that are recorded. For example, there are enigmatic differences between the compositions of biominerals versus inorganic counterparts that are grown under similar environmental conditions. There are also differences between the compositions of calcified biominerals from similar species that co-existed in similar environments. In the latter case, these "vital effects," may be due to species-specific physiological controls over mineralization. Given that multiple pathways to biomineral formation are possible, one explanation for vital effects may be that differences reflect the predominant mineralization process— such as when calcite forms by a classical step growth process (Teng et al., 1998) versus transformation from an initial amorphous phase (Weiner et al., 2003; Bentov et al., 2006; Wombacher et al., 2011; Wallace et al., 2012).

For example, calcite grown by classical ion-by-ion attachment would be expected to record the composition of the individual components that are incorporated at the crystal surface. In contrast, signals that result from a mineralization process involving ACC may reflect the conditions of formation for the initial amorphous phase or be modified during the transformation to calcite. Therefore, the transformation itself may act as a gatekeeper that determines biomineral composition and, by extension, the trends that are measured in proxies. To decipher this complexity, a process-based understanding of nonclassical mineralization is critically needed. From this mechanistic basis, a robust approach for reconstructing past environmental conditions may become possible.

Two end-member interpretations have emerged in ongoing discussions of the process by which ACC transforms to calcite. Using evidence from microscopic and spectroscopic studies of skeletal structure, the first proposes that ACC transforms by a solid state process that involves dehydration and the structural rearrangement of ACC within membrane-bound compartments into crystalline products (Beniash et al., 1999; Politi et al., 2008; Weiner et al., 2011; Gal et al., 2013). By this process, one expects the elemental and isotopic signatures measured in the final calcite to record conditions at the time of ACC formation. At the other end of the transformation spectrum, in vitro evidence indicates that accumulated ACC transforms by dissolving and reprecipitating as calcite (Pontoni et al., 2003; Lee et al., 2007; Han et al., 2008; Wolf et al., 2008; Bots et al., 2012; Hu et al., 2012; Gal et al., 2013; Ihli et al., 2013). In this case, the final calcite product records the conditions of the local environment at the time of transformation.

These end-member interpretations are complicated by recent *in situ* TEM observations of physical contact between ACC and the crystalline phase during

transformation that indicate both processes may occur simultaneously (Nielsen et al., 2014). This suggests a third possibility for the transformation that involves a combination of the solid state and dissolution-reprecipitation processes. These previous studies provide important insights but a definitive physical picture is elusive. To our knowledge, there is no chemical evidence to directly discern which of these processes is predominant.

This study reports direct chemical evidence regarding the ACC to calcite transformation process which allows us to determine when and where isotopic signatures are recorded. We designed a set of experiments that produce ACC from solutions labeled with stable isotopes of ^{43}Ca and ^{25}Mg, then monitored the exchange of ions between solution, ACC and calcite during the transformation process. The rate of the ACC to calcite transformation was qualitatively regulated by including experiments conducted in solutions with three ratios of Mg/Ca. Measurements of isotope distributions show the transformation involves extensive interaction with the local solution. Little of the original ACC isotopic signature is retained, particularly for the higher Mg experiments that have longer transformation times. For the conditions of these longer duration experiments, the signatures after transformation fall on a mixing line between the ACC and solution end-members. These findings indicate the transformation is dominated by a dissolution-reprecipitation process and suggest the signatures contained in the calcite crystals record the local solution conditions at the time of transformation.

3.3. METHODS

3.3.1. Synthesis of ACC and transformation to calcite

ACC was synthesized by a modified version of the widely used ammonium carbonate decomposition method (Gruzensky, 1967; Addadi et al., 1985; Paquette et al., 1995; Han et al., 2008; Wang et al., 2009; Wang et al., 2012). Polystyrene well plates were used to conduct the reactions, with each well containing 3 ml of solution. Each well also contained one glass coverslip (1.4 cm diameter), with the whole assembly placed inside a sealed glass jar at 100% humidity. The initial calcium composition of the solution in each well was 10 mM ($CaCl_2 \cdot 2H_2O$, Sigma Aldrich, >99%, dissolved in 18.2 MΩ·cm ultrapure water). To explore the influence of magnesium on ACC growth and transformation, the experimental design used initial solution Mg/Ca ratios of 2.0, 5.0, or 6.0 (mol/mol) through the addition of a stock solution of 1.0 M Mg^{2+} ($MgCl_2 \cdot 6H_2O$, Sigma Aldrich, ≥99%). For this synthesis method, solution Mg/Ca drifts during precipitation due to reservoir (Rayleigh) processes, hence the reference to "initial Mg/Ca". Supersaturation was achieved by adding 10 g $(NH_4)_2CO_3$ (Sigma Aldrich) to a separate and constantly stirred 20 mL volume of water in the glass jar. As NH_3 and CO_2 gases diffused from the $(NH_4)_2CO_3$ and into each well, ACC precipitated from the calcium and magnesium chloride solutions onto the glass coverslips and sides of wells, forming within minutes of the start of the reaction for all conditions.

The transformation of ACC to calcite was monitored using an optical microscope. Parallel experiments, where solids were removed at specific time points, were conducted to characterize the materials. For all experimental conditions, the ammonium carbonate source was removed before the transformation to calcite began. The onset of

transformation varied from 2-5 hours to 16-24 hours for solutions with initial Mg/Ca ratios of 2.0 and 5.0-6.0, respectively. Upon complete transformation (about 5 days), the glass coverslips with calcite were removed, rinsed in ethanol, and dried in air. The crystalline products were identified as calcite or aragonite by Raman spectroscopy on a JY Horiba U1000 spectrometer (Wang et al., 2012). SEM images of the crystals (solution side) were acquired on a LEO (Zeiss) 1550 field emission scanning electron microscope under high vacuum and 5 kV accelerating voltage.

3.3.2. Isotope labeling using ^{43}Ca and ^{25}Mg

A subset of the wells was filled with isotopically labeled solutions. Enriched isotope spikes (Oak Ridge National Lab) were dissolved, and mixed with natural abundance reagents to achieve a simultaneous 3.8-fold enrichment of ^{43}Ca and 7.9-fold enrichment of ^{25}Mg for each solution. These large enrichments were chosen for two reasons: (1) they provide a unique label that is easily measured with NanoSIMS, and (2) for enrichments of several thousand permil, we assume natural fractionation effects are insignificant, where fractionation between the solution and calcite during mineralization has an approximate magnitude of -3 to 0‰ (Galy et al., 2002; Chang et al., 2004; DePaolo, 2011; Wombacher et al., 2011; Li et al., 2012). This means that any fractionation that occurred during mineralization was too small to explain the isotopic signatures we measured in this study. The isotopic composition of the initial growth solutions (**Table 3.1**) were confirmed using an Elan DRC-II quadrupole inductively coupled plasma mass spectrometer (Q-ICP-MS; Perkin Elmer). Instrumental mass fractionation during Q-ICP-MS analysis was corrected using bracketing of enriched and

natural abundance standards of known isotopic composition. The standards were the same as described in Fernandez et al. (2010).

Table 3.1: Summary of solution isotope enrichments. The $^{43}Ca/^{40}Ca$ and $^{25}Mg/^{24}Mg$ of natural and spiked solutions are obtained from Q-ICP-MS analysis.

Initial Mg/Ca ratio	$^{43}Ca/^{40}Ca$			$^{25}Mg/^{24}Mg$		
	Natural	Spiked	Enrichment	Natural	Spiked	Enrichment
2.0	0.00138	0.00516	3.8-fold	0.129	1.012	7.9-fold
5.0	0.00138	0.00454	3.3-fold	0.129	1.005	7.8-fold
6.0	0.00138	0.00510	3.7-fold	0.129	1.022	7.9-fold

3.3.3. Experimental design

The experimental design used four wells run in parallel for each Mg/Ca solution ratio (2.0, 5.0 and 6.0 mol/mol) as shown in **Fig. 3.1A**. Two of the wells were designed to act as controls with the remaining two wells used during different stages of the experimental treatment. The first control well contained natural abundance reagents during the entire experiment so that the ACC precipitated and transformed to calcite without artificially enriched isotopes (**Fig 3.1, first column**). A second control well was isotopically labeled. These experiments contained a solution enriched in both ^{43}Ca and ^{25}Mg isotopes for the entire experiment. Since the ACC in this control precipitated from an isotopically enriched solution and subsequently transformed to calcite in the same enriched solution, we would expect both the ACC and calcite to be isotopically enriched regardless of transformation pathway (**Fig 3.1, last column**).

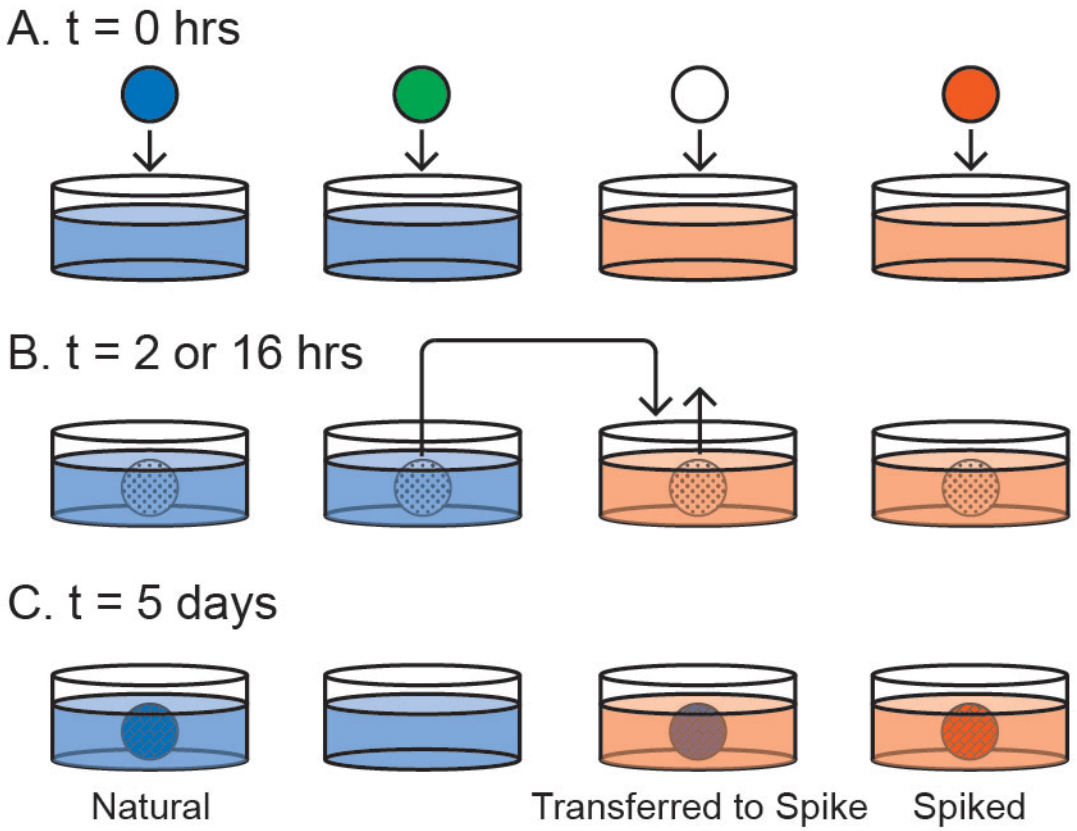

Fig. 3.1: Experimental design for ^{43}Ca and ^{25}Mg isotope labeling of solutions and solid phases. Four wells were filled with solutions that contained a natural abundance of isotopes (blue solutions, columns 1 and 2) or an enriched isotope abundance (red solutions, columns 3 and 4). Solids forming from the well plate in column 1 correspond to the natural abundance control. In contrast, column 4 corresponds to a control where the solid is isotopically labeled. The two well plates in the columns 2 and 3 were used for the experimental treatment. (A) At time = 0, a glass coverslip was placed in each well and ACC was allowed to precipitate after adding the carbonate source. (B) Before the onset of transformation to calcite, which occurred at 2-5 hours (for Mg/Ca = 2.0) or 16-24 hours (Mg/Ca = 5.0 and 6.0), the glass coverslip in the enriched well (column 3) is removed and replaced by the coverslip from the natural isotope abundance well. (C) After five days, the ACC completely transformed. Collectively this experimental design produces three types of samples for analysis: the natural and spiked controls and the transferred (natural to spiked) treatments.

The experimental treatment used two wells, one containing the same natural abundance solution as the natural abundance control, while the other well began with the same solution as the isotopically spiked control (**Fig 3.1**, second and third columns). Unlike the controls, where each glass coverslip was kept in the same solution during the

whole experiment, coverslips were transferred between the different solutions after ACC precipitated but before the ACC transformed to calcite (**Fig 3.1B**). The timing of this transition was monitored using an optical microscope. The coverslip transferred from the natural abundance solution to the enriched solution was the focus for subsequent analysis in this study. In contrast, the coverslip that started in the enriched solution was removed before the ACC to calcite transition. The sole purpose of this coverslip was to ensure that the two wells had similar calcium and magnesium concentrations at the time of transfer.

The initial Mg/Ca solution conditions of 2.0 produced approximately half the amount of ACC on the glass coverslips as did the Mg/Ca conditions of 5.0 and 6.0. All coverslips were transferred to the isotopically enriched solutions for the transformation and returned to the glass jar with the ammonium carbonate source removed (**Section 3.3.1**). These samples were allowed to transform for 5 days. A second set of experiments replicated the entire array of conditions (2.0, 5.0, or 6.0 Mg/Ca ratios and natural, spiked, or transferred ACC).

3.3.4. NanoSIMS spot analysis

The calcite products were analyzed at sub-micron spatial resolution using NanoSIMS, a powerful surface analysis tool that that can provide detailed measurements of elemental and isotopic composition. Samples were prepared for isotopic analysis by embedding calcite crystals from each experimental condition into indium metal. A 1 inch, 19-well sample holder was filled with melted In and, upon cooling, flattened using a hydraulic press at 10,000 psi for 10 seconds. For each condition, calcite crystals were transferred to the indium by pressing a coverslip upside down into an indium-filled well.

This exposed their flat undersides for analysis. All samples and standards were sputter-coated with a 30.5 nm thick gold film prior to analysis.

Isotope measurements were performed on the CAMECA NanoSIMS-50L (California Institute of Technology) using a duoplasmatron (O^-) source. The primary beam spot (measured as roughly 540 nm, full width and half max) was rastered during analysis to measure a well-defined square region with sides 2 microns in length. Total counts of ^{40}Ca, ^{43}Ca, ^{24}Mg, and ^{25}Mg were collected over 4.25 minutes for each spot analysis, including 75 seconds of presputtering to remove the gold coating followed by 60 cycles of 3 seconds duration each. The drift across cycles for each spot was consistent across the run and relatively reproducible with the standards. Single spot analyses were performed on 6-10 calcite crystals for each condition, identified during analysis using a CCD camera and post-analysis using SEM for each experimental condition (for 81 total spots). Standards were measured regularly to bracket the samples, to correct for instrumental mass fractionation, and to establish accurate Mg/Ca. Additionally, a linear drift correction for instrumental mass fractionation was generated using all standards and natural abundance samples (assuming the solutions contained natural isotopic abundance). For all samples, the resulting crystals collected an approximately constant number of counts (within 20% and 5% relative error for ^{43}Ca and ^{25}Mg, respectively) across 60 measurement cycles (**Section 3.4.2**). This suggested a homogeneous depth distribution of the $^{43}Ca/^{40}Ca$ and $^{25}Mg/^{24}Mg$ within the calcite crystals.

The magnesium content of the calcite was measured by NanoSIMS by calibrating $^{24}Mg/^{40}Ca$ to $\%MgCO_3$ of Mg-calcite and dolomite standards. The results from all sample conditions (natural, spiked, and transferred) were averaged across initial Mg/Ca solution

ratios and fall within one standard error of previous %Mg estimates from [104] peak shifts on XRD (**Table 3.2**) (Wang et al., 2012). Three additional calcite standards were also measured throughout the NanoSIMS analysis to establish accurate Mg/Ca ratios, as described in Gabitov et al. (2013). The three calcite standards were Blue Calcite (Mg/Ca = 3.75); UC Irvine Calcite (Mg/Ca = 3.446); Rensselaer Polytechnic Calcite (Mg/Ca = 0.396) and one dolomite standard (Mg/Ca = 1.00). The NanoSIMS was advantageous for this study over bulk chemical analysis because it enabled us to directly resolve the compositions of single calcite crystals without the bias of the late stage aragonite that formed (Wang et al., 2012) and without the averaging effects of bulk analysis.

Table 3.2: The Mg content (mol% $MgCO_3$) of calcite averaged across all isotope conditions (natural, spiked, and transferred to spike calcites) is obtained from NanoSIMS and compared to XRD estimates from previous work using the same growth conditions. Errors are reported as one standard deviation of all crystals analyzed.

Initial Mg/Ca ratio of solution	Mg content (mol% $MgCO_3$)	Mg content (mol% $MgCO_3$)[a]
2.0	19±10	12.2±0.2
5.0	41±15	35.2±0.8
6.0	51±17	36.6±1.3

[a](Wang et al., 2012)

Following NanoSIMS analysis, SEM images of the embedded crystals were collected to identify spot locations and crystal integrity. By comparing the coordinates of the spot analysis to the ion beam marks in the SEM images, we confirmed the polymorph associated with each spot analysis. This screening allowed us to reject data from crystals that were unidentifiable or identified as aragonite (14 spots). An additional 5 spots were rejected because they had low counts, which were attributed to rough topography or missing crystals. After data filtering, a total of 62 spot measurements remained with 3 to 10 spots for each experimental condition. It was not possible to determine the order of crystal formation within a given sample.

3.4. RESULTS

3.4.1. ACC precipitation and transformation to Mg-calcite

For all experiments, the ACC precipitated within minutes of adding the ammonium carbonate source. Its subsequent transformation into calcite slowed with increasing Mg content of the solution as reported previously (Folk et al., 1975; Reddy et al., 1976; Loste et al., 2003; Wang et al., 2009; Wang et al., 2012; Xu et al., 2013). For experiments conducted in the lowest initial solution Mg/Ca ratio of 2.0, the transformation began after 2 hours to produce crystals with an elongated, often dumbbell morphology reported previously (Han et al., 2003; Loste et al., 2003) (**Fig. 3.2AC**) and contained 19±10 mol% $MgCO_3$ (**Table 3.2**). For experiments conducted in the 5.0 and 6.0 Mg/Ca solutions, the transformation began at 16 to 24 hours, and a larger amount of ACC precipitate was produced on the coverslips. The resulting calcites grew with characteristic spherical to botryoidal macroscopic morphologies (**Fig. 3.2BD**) as reported by Wang et al. (2012). Composition analyses showed the 5.0 and 6.0 Mg/Ca solutions produced calcites that contained 41±15 and 51±17 mol% $MgCO_3$, respectively (**Table 3.2**). The complete transformation of ACC to calcite in some experiments required up to 5 days.

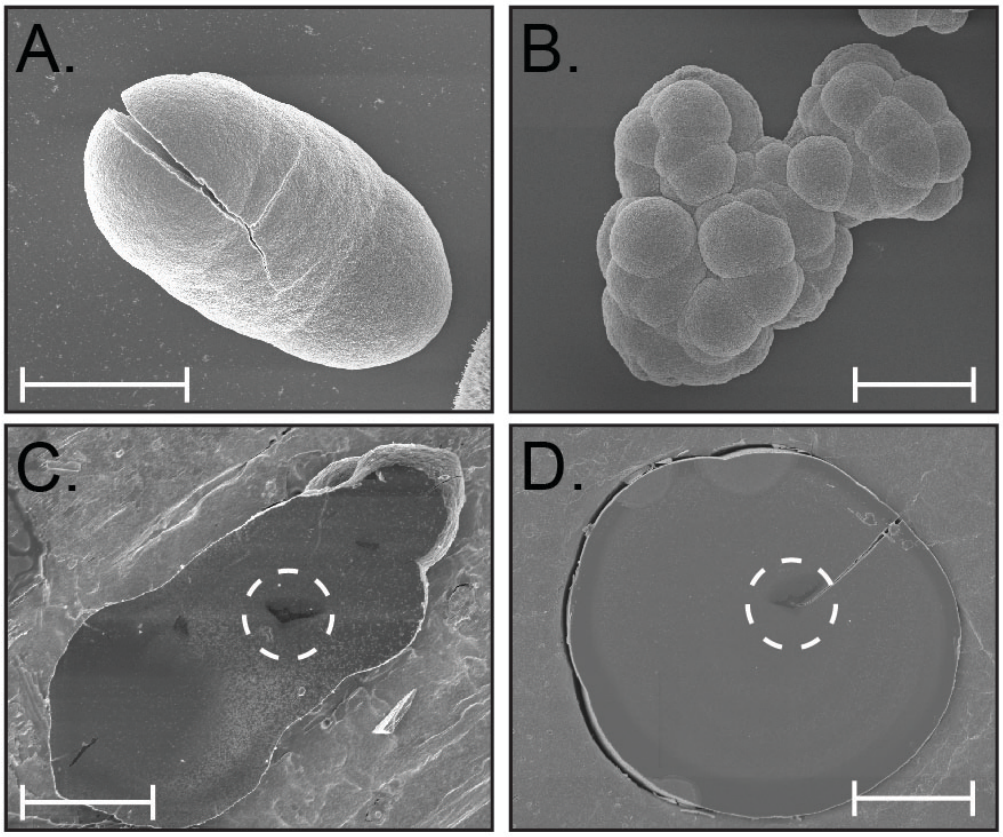

Fig. 3.2: SEM images of representative calcite morphologies. (A and C) initial Mg/Ca = 2.0 produces calcite with an elongated to dumbbell morphology; (B and D) initial Mg/Ca = 5.0 produces spherical to botryoidal calcite. Crystals pressed into indium present a flat underside (C and D) suitable for NanoSIMS analysis. The white dashed circle marks a darker "V" shape representing beam damage around each ~2 um^2 analysis area. Scale bars = 20 μm.

Under all conditions, the transformation was followed by the nucleation and growth of secondary aragonite as confirmed by Raman and XRD analyses. This polymorph grew with an acicular morphology as individual spindles or as overgrowths onto the high-Mg calcite. This observation is consistent with previous studies using this method (Raz et al., 2000; Wang et al., 2012).

3.4.2. Isotopic analysis of controls and treatments

In the control experiments, natural abundance solutions resulted in natural abundance calcite crystals, while enriched solutions produced enriched calcite crystals, as expected. In greater detail, the raw number of ^{43}Ca and ^{25}Mg counts collected for a typical spot of a natural abundance calcite (**Fig. 3.3A**) were significantly lower than calcites from a spiked experiment (**Fig. 3.3B**). To evaluate the data collected for each spot analysis, we determined the isotope ratios ($^{43}Ca/^{40}Ca$ and $^{25}Mg/^{24}Mg$) for each of 60 measurement cycles as illustrated in **Fig. 3.3C**, then averaged these ratios to obtain one set of mean $^{43}Ca/^{40}Ca$ and $^{25}Mg/^{24}Mg$ values for each crystal (**Table C.1**). A similar process was used to produce average isotope ratios of each crystallite for all control and experimental treatments.

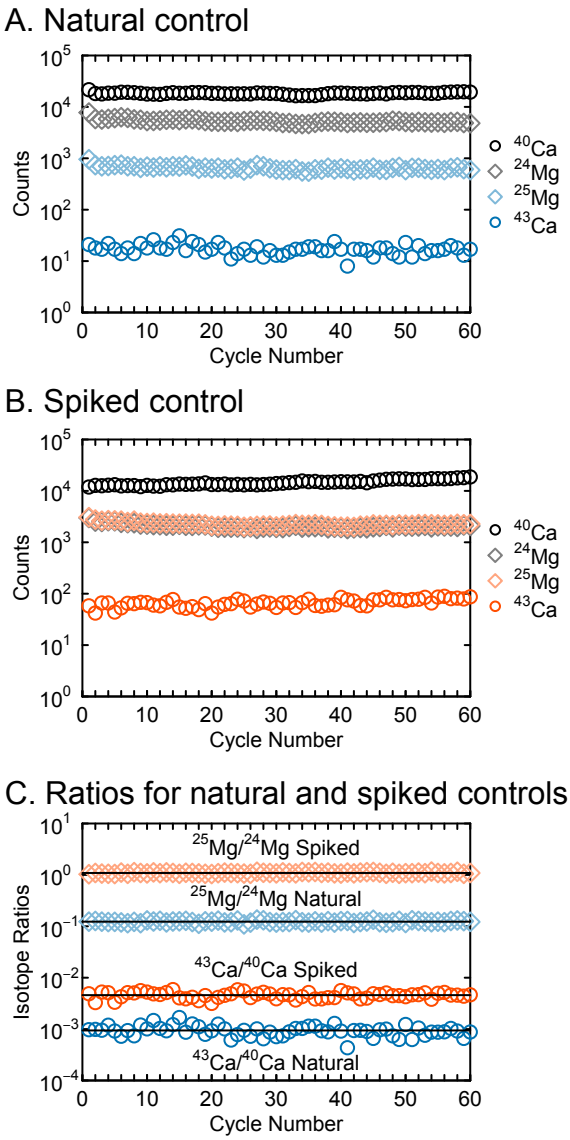

Fig. 3.3: Typical NanoSIMS spot analysis show the typical isotope counts collected over 60 cycles of measurements for two high-Mg calcite crystals (initial Mg/Ca = 5.0) (A) Natural abundance control. (B) Spiked control shows higher ^{25}Mg and ^{43}Ca counts for calcites that transformed from ACC in a spiked solution. (C) Calculated isotope ratios for the natural and spiked controls in A and B. The spiked calcite control shows ^{43}Ca and ^{25}Mg enrichments that are consistent with solution isotope abundance (compare to **Table 3.1**).

In a plot of measured ^{43}Ca/^{40}Ca vs. ^{25}Mg/^{24}Mg (**Fig. 3.4**), the natural abundance and spiked controls define two isotopically distinct end-members. First, the *natural abundance* controls have isotopic ratios that are clustered within a small range of values.

This pattern is found for all initial Mg/Ca solution values (blue squares in **Fig. 3.4ABC**). The *spiked controls* cluster in a region that is very distinct from the natural abundance controls (red triangles in **Fig. 3.4ABC**). For the higher Mg/Ca experiments, the isotope ratio of the spiked control is more variable (**Fig. 3.4BC**). Since few physically reasonable processes could result in this sort of fractionation, we assume this variability is caused by analytical issues. Indeed this variability could be related to the fact that only three viable measurements remained for the spiked controls for the Mg/Ca of 6.0 solutions after screening the data using the stated criteria (**Section 3.3.4**) and most of these crystals were intimately associated with late-stage aragonite. Even including all of these points, the variability is small compared to the isotopic difference between the natural abundance and enriched controls.

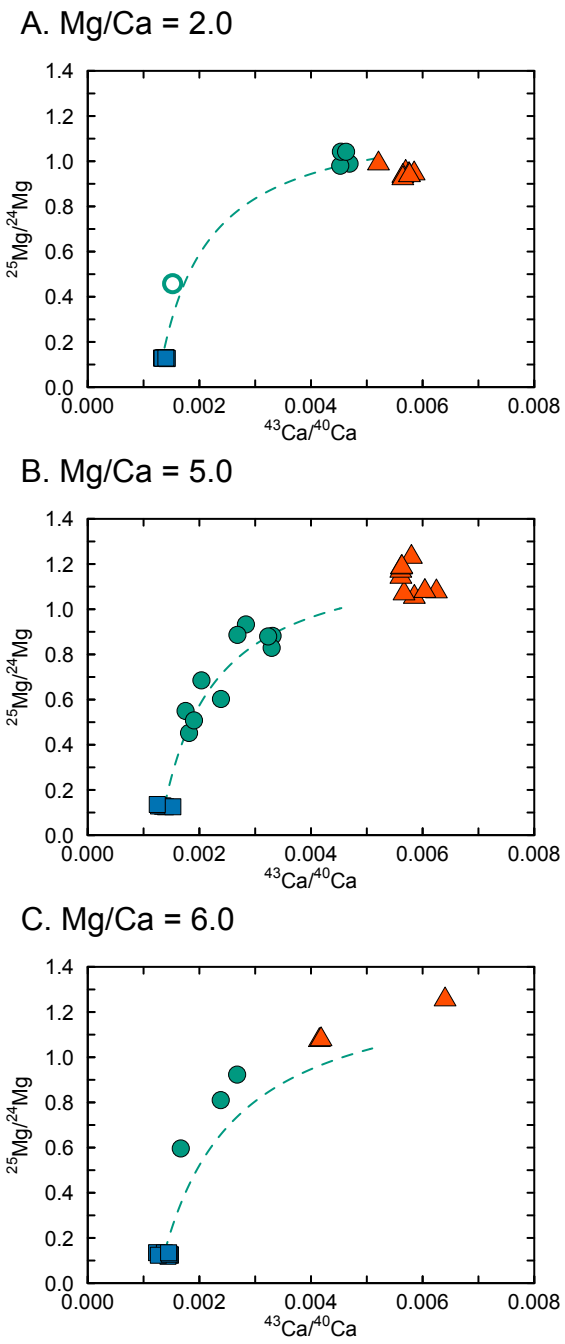

Fig. 3.4: The isotope ratios determined from calcites for the natural abundance controls (blue squares), the spiked controls (red triangles), and experimental treatments that began as ACC in natural abundance solutions and were transferred to spiked solutions for transformation to calcite (green circles). Three solution compositions were used: (A) Mg/Ca = 2.0, (B) Mg/Ca = 5.0, and (C) Mg/Ca = 6.0. Predictions of mixing model for each solution composition are shown as a dashed line (**Section 3.5.1**).

Recall the treatment experiments began by precipitating the ACC in natural abundance solutions and this material was transferred to the spiked solutions for the subsequent transformation to calcite (**Section 3.3.3**). Experiments that began in Mg/Ca of 2.0 produced calcite (five of the six crystals) that exhibit a narrow range of isotopic ratios (green circles in **Fig. 3.4A)** and have compositions similar to the spiked controls with the exception of one crystal (open green circle in **Fig 3.4A**). In contrast, the higher Mg solutions produced calcite crystals with isotopic ratios that are intermediate between the natural abundance and spiked controls (**Fig 3.4BC**). The 10 measurements from experiments that began with Mg/Ca of 5.0 solutions appear to show a mixing trend which will be discussed in detail below. A similar trend is indicated by the Mg/Ca of 6.0 experiments (**Fig 3.4C**) for the three viable measurements. Sample number was limited because of extensive precipitation of late-stage aragonite.

3.5. DISCUSSION

3.5.1. Transformation pathways and mixing model

We use plots of $^{43}Ca/^{40}Ca$ vs. $^{25}Mg/^{24}Mg$ to determine which pathways are most important during the ACC to calcite transformation. Recalling that the treatment experiment produced ACC from a natural abundance solution (lower left end-member in **Fig. 3.4ABC**) and that this ACC was moved to an enriched solution for transformation (upper right end-member in **Fig. 3.4ABC**), then each of the four possible transformation scenarios are possible for how the data for the treatment calcite should plot: First, we consider that ACC transforms to calcite by a strictly solid state process, thus retaining the original natural abundance signature. In this case the resulting calcite would plot in the lower left corner together with the natural abundance control. None of the analyzed calcites from our treatment experiments are consistent with this pathway.

Second, the ACC transforms in the spiked solution by complete dissolution, but the amount of natural abundance ACC added to the solution during this dissolution process is small, resulting in little to no change to the solution isotope ratio. In this case, subsequent calcite reprecipitation would yield a solid that is similar to the isotopically enriched control. This pathway can explain most of the data from the low Mg/Ca experiments (**Fig. 3.4A**), but not the other treatments.

The third and fourth transformation scenarios involve mixing between the two end-members. All four possibilities are illustrated in **Fig. 3.5**. The dashed curves (**Fig. 3.5)** were constructed assuming mixing between two end-members with different isotopic compositions and different Mg/Ca ratios using a simple binary hyperbolic function (**Appendix C2**) (Vollmer, 1976; Langmuir et al., 1978). When the mixing relationships are plotted in $^{43}Ca/^{40}Ca$ vs. $^{25}Mg/^{24}Mg$ space, the end-member locations in **Fig. 3.5** depend upon isotope composition, but the curvature of the mixing relationship depends on the elemental composition of the end-members. For example, mixing with a high Mg/Ca end-member would tend to change the magnesium isotope ratio more rapidly relative to calcium isotopes than mixing with a low Mg/Ca end-member. Because ACC, calcite, and the solution in each well have very different Mg/Ca ratios, different mixing scenarios between these end-members will plot along lines with different curvature. Thus, while each of the mixing scenarios has process-specific concavity, the *degree of curvature* for both mixing trends is dependent upon the Mg/Ca ratio of an experiment.

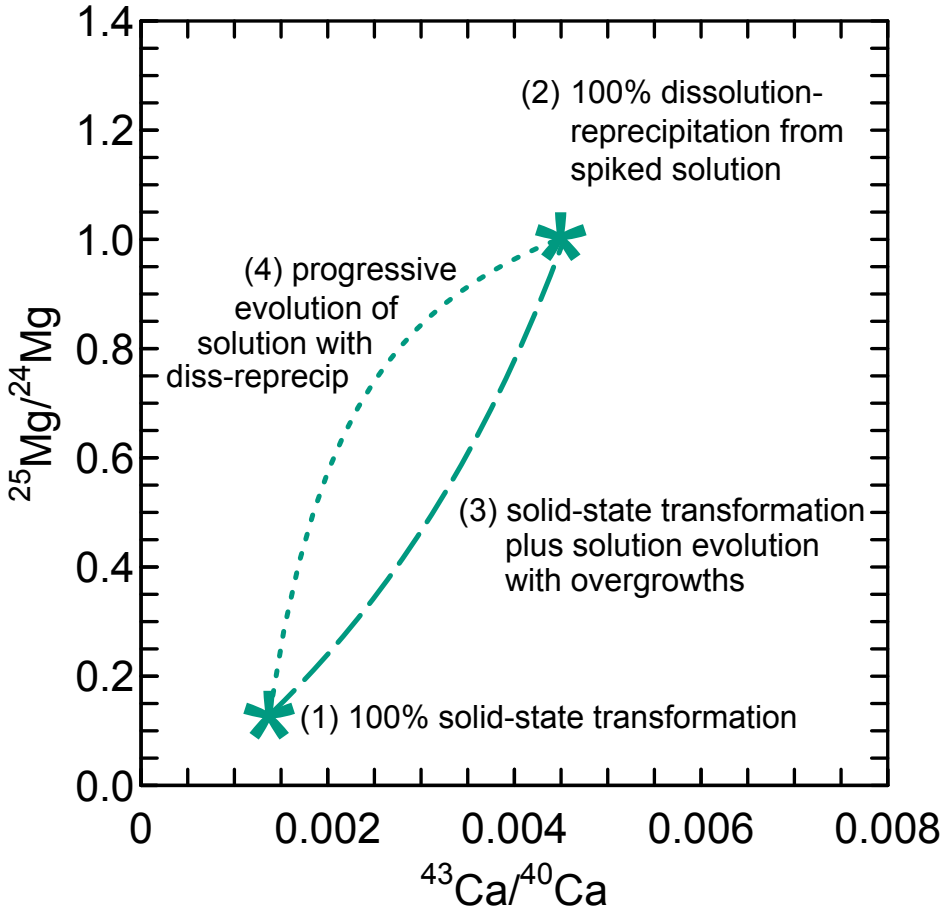

Fig. 3.5: Predictions of mixing model show isotope-specific signatures expected for calcite that transforms from ACC: (1) complete solid state rearrangement; (2) complete dissolution-reprecipitation; (3) combination of solid state transformation and partial overgrowth of calcite by reprecipitation; and (4) combination of dissolution-reprecipitation where the progressive dissolution of ACC affects solution composition. Comparisons to the experimental measurements (**Fig 3.4ABC**) indicate the transformation occurs by dissolution-reprecipitation. Mixing lines in this image are calculated for solutions with Mg/Ca=5.0.

The first mixing scenario we consider is a transformation process involving a combination of both solid state and dissolution-precipitation processes. This scenario would produce a concave up curve because the magnesium isotope signature of the solid mixture is dominated by the high Mg/Ca ACC end-member (**Fig. 3.5**). One way to visualize this transformation process is that some fraction of calcite is formed by an early

stage solid state transformation and the remainder is produced by dissolution-reprecipitation as a later stage overgrowth from solution. This transformation process is important to consider because it would likely result in the intimate association of crystallites whose size could be below the resolution of the NanoSIMS analysis. Comparing this scenario with our data, none of our experiments follow a concave-up mixing trajectory.

In the final scenario, we consider a situation where the composition of the solution evolves due to dissolution of ACC during a dissolution-reprecipitation pathway. This will occur if a large amount of ACC dissolves relative to the amount of solution that is present. In this scenario, the mixing curve would be concave down, because the solution has a higher Mg/Ca than ACC, with the magnesium isotope signature of the mixture dominated by the spiked solution end-member. During calcite precipitation, the crystal will capture the isotope ratio of the surrounding solution, thus the isotope ratios of different calcite crystals will plot along a mixing curve that reflects the evolving solution composition. The process is entirely dissolution-reprecipitation but the calcite is growing from a changing solution environment.

3.5.2. Qualitative insights for the transformation process

Returning to the experimental data in **Fig. 3.4ABC,** the measurements show a distinct concave down trend for all solution compositions, which suggests that the transformation is a predominantly dissolution-reprecipitation process (e.g. **Fig. 3.5**). There is no evidence for a solid state transformation within the resolution of these data.

For experiments that began with Mg/Ca = 2.0 (**Fig 3.4A**), the $^{25}Mg/^{24}Mg$ and $^{43}Ca/^{40}Ca$ values measured in the calcite products are clustered near and *to the left* of the

composition of the spiked solutions where they transformed. This indicates extensive dissolution-reprecipitation (e.g. discussion of **Fig 3.5**). The offset from the spiked end-member (control) is likely due to mixing with the natural abundance isotopes that are released during dissolution of the initial ACC. This shift is small because the amount of ACC transferred is small (see **Section 3.3.2**) and the complete transformation in these low Mg experiments occurred within a short period. The products thus present a cluster of similar, enriched compositions.

In contrast, the treatments that began with the higher solution Mg/Ca ratios (5.0, 6.0) produce calcite crystals with a span of isotopic ratios (**Fig. 3.4BC).** These data exhibit a mixing trend with the distinct concave down curvature suggesting a transformation process that is dominated by dissolution and reprecipitation. The values in **Fig. 3.4B** suggest good agreement with the predictions of the theoretical model (compare experimental measurements with dashed line).

To understand the physical basis for the span of measured isotopic ratios in **Fig. 3.4BC**, recall the higher Mg solutions required a longer time for the complete transformation of ACC to calcite and produced twice the amount of ACC material on the coverslips. Thus, a greater mass of ACC relative to the solution volume was transferred into the well (**Section 3.3.2**), which introduced a larger mass of the natural abundance isotopes. Upon transformation in the spiked solutions, the dissolution of this larger quantity of material induces an increasingly greater shift in the isotope ratios of the solution over the course of the transformation to calcite. Thus, we suggest the span of compositions measured in these experiments is the compounded effect of larger amounts

of ACC on the coverslips transferred to the spike solution and the progressively greater shift in local solution composition during the longer time to transformation.

At the highest Mg/Ca solutions (**Fig. 3.4BC**), the mixing model has the same curvature but a small and systematic offset from the experimental measurements. Recall the endpoint of the model is governed by the solution isotope composition (**Section 3.5.1**) and the spiked control measurements exhibited a higher variability than the natural control measurements (**Section 3.4.2**). Thus, we attribute the offset in the mixing model to analytical uncertainties in the isotopic compositions of the solution or the spiked controls. While this offset limits quantitative interpretation of the data, the mixing trend exhibited by the data supports the explanation that the ACC to calcite transformation is a predominantly dissolution-reprecipitation process for the conditions of these experiments and the values measured in the final calcite products record the local solution environment at the time of transformation.

3.5.3. Implications

For the conditions of this experimental study, the formation of calcite from an inorganic ACC intermediate occurs by a dissolution-reprecipitation process. The isotopic ratios contained in the initial ACC are largely replaced to produce calcites with signals that reflect the solution composition at the time of transformation. When the amount of ACC that precipitates is relatively large compared to the size of the solution reservoir, the calcite compositions plot on a mixing curve that record a mixture between dissolved ACC and the solution. Experiments that require a longer transformation period (through higher Mg/Ca ratios) are qualitatively associated with a greater spread of isotopic compositions. We interpret this trend as the temporal evolution of solution composition.

Our observations of the isotopic co-evolution of solution and solid imply a similar evolution in the elemental composition of the final products is also active during the transformation.

The findings could help us understand what controls biomineral compositions for situations where mineralization involves an intermediate phase. For example, a solid state transformation during biomineralization would lock the distinct geochemical signals associated with ACC into the final skeleton (ex. high Mg/Ca) such that the proxy behavior would be strongly influenced by the initial ACC composition. Our study, however, shows that when the transformation is dominated by dissolution-reprecipitation, the composition of the ACC can be completely erased or partially remodeled such that signals in the final calcite bear little resemblance to the initial conditions. While the geochemical implications of a dissolution-reprecipitation process are clear, the question remains whether this transformation process is generally followed during biomineralization or whether this process is particular to our inorganic experiments.

Insights from this study also raise the point that final mineral composition is influenced by the amount of ACC relative to the volume and concentration of elements in the calcifying solution. Compositional variations in the calcite products are greater when the amount of ACC transferred is large relative to the reservoir. This experimental observation leads us to ask how the size of a reservoir in a mineralizing biological system influences final skeletal composition. While this implies a complex sensitivity to local reservoir conditions, such a dependence suggests the extent to which there is water available would change the end point composition on the mixing line. Moreover, this may have the potential to explain some aspects of proxy variability that occur in synthetic

crystals and biominerals. For example, uncertainties that are presently interpreted as random noise, experimental error, or vital effects, may reflect a co-evolution of reservoir and products over the duration of the transformation.

Finally, it is intriguing to consider the reverse question of whether the skeletal products of carbonate-producing organisms contain compositional trends that can inform the biomineralization pathways. One may be able to use isotopic signatures to reconstruct pathways when combined with additional information about an organism. By integrating insights from multiple pathways to mineralization with the host of environmental, chemical and biological factors that influence growth, a robust physical basis for interpreting and predicting biomineral compositions may become possible.

3.6. REFERENCES

Addadi L., Raz S. and Weiner S. (2003) Taking advantage of disorder: amorphous calcium carbonate and its roles in biomineralization. *Adv. Mater.* **15**, 959-970.

Addadi L., Vidavsky N. and Weiner S. (2012) Transient precursor amorphous phases in biomineralization. In the footsteps of Heinz A. Lowenstam. *Z. Kristallogr.* **227**, 711-717.

Addadi L. and Weiner S. (1985) Interactions between acidic proteins and crystals: Stereochemical requirements in biomineralziation. *Proc. Natl. Acad. Sci.* **82**, 4110-4114.

Al-Sawalmih A., Li C., Siegel S., Fratzl P. and Paris O. (2009) On the stability of amorphous minerals in lobster cuticle. *Adv. Mater.* **21**, 4011-4015.

Beniash E., Addadi L. and Weiner S. (1999) Cellular control over spicule formation in sea urchin embryos: A structural approach. *J. Struct. Biol.* **125**, 50-62.

Bentov S. and Erez J. (2006) Impact of biomineralization processes on the Mg content of foraminiferal shells: A biological perspective. *Geochem. Geophy. Geosy.* **7**, 1-11.

Bots P., Benning L.G., Rodriguez-Blanco J.-D., Roncal-Herrero T. and Shaw S. (2012) Mechanistic insights into the crystallization of amorphous calcium carbonate (ACC). *Cryst. Growth Des.* **12**, 3806-3814.

Chang V.T.C., Williams R.J.P., Makishima A., Belshawl N.S. and O'Nions R.K. (2004) Mg and Ca isotope fractionation during CaCO3 biomineralisation. *Biochem. Biophys. Res. Commun.* **323**, 79-85.

Chase Z., Anderson R.F. and Fleisher M.Q. (2001) Evidence from authigenic uranium for increased productivity of the glacial subantarctic ocean. *Paleoceanography* **16**, 468-478.

DePaolo D.J. (2011) Surface kinetic model for isotopic and trace element fractionation during precipitation of calcite from aqueous solutions. *Geochim. Cosmochim. Acta* **75**, 1039-1056.

Dillaman R., Hequembourg S. and Gay M. (2005) Early pattern of calcification in the dorsal carapace of the blue crab, Callinectes sapidus. *J. Morphol.* **263**, 356-374.

Emiliani C. (1954) Depth habitats of some species of pelagic foraminifera as indicated by oxygen isotope ratios. *Am. J. Sci.* **252**, 149-158.

Epstein S., Buchsbaum R., Lowenstam H.A. and Urey H.C. (1953) Revised carbonate-water isotopic temperature scale. *Geol. Soc. Am. Bull.* **64**, 1315-1326.

Fernandez D.P., Gagnon A.C. and Adkins J.F. (2010) An isotope dilution ICP-MS method for the determination of Mg/Ca and Sr/Ca ratios in calcium carbonate. *Geostand. Geoanal. Res.* **35**, 23-37.

Folk R.L. and Land L.S. (1975) Mg/Ca ratio and salinity: Two controls over crystallization of dolomite. *AAPG Bull.* **59**, 60.

Frank M., Gersonde R., van der Loeff M.R., Bohrmann G., Nürnberg C.C., Kubik P.W., Suter M. and Mangini A. (2000) Similar glacial and interglacial export bioproductivity in the Atlantic Sector of the Southern Ocean: Multiproxy evidence and implications for glacial atmospheric CO2. *Paleoceanography* **15**, 642-658.

Gabitov R.I., Gagnon A.C., Guan Y., Eiler J.M. and Adkins J.F. (2013) Accurate Mg/Ca, Sr/Ca, and Ba/Ca ratio measurements in carbonates by SIMS and NanoSIMS and

an assessment of heterogeneity in common calcium carbonate standards. *Chem. Geol.* **356**, 94-108.
Gal A., Habraken W., Gur D., Fratzl P., Weiner S. and Addadi L. (2013) Calcite crystal growth by a solid-state transformation of stabilized amorphous calcium carbonate nanospheres in a hydrogel. *Angew. Chem. Int. Ed.* **52**, 4867-4870.
Galy A., Bar-Matthews M., Halicz L. and O'Nions R.K. (2002) Mg isotopic composition of carbonate: insight from speleothem formation. *Earth Planet. Sci. Lett.* **201**, 105-115.
Gruzensky P.M. (1967) Growth of calcite crystals. *Crystal growth*, 365-367.
Han T.Y.-J. and Aizenberg J. (2008) Calcium carbonate storage in amorphous form and its template-induced crystallization. *Chem. Mater.* **20**, 1064-1068.
Han Y.-J. and Aizenberg J. (2003) Effect of magnesium ions on oriented growth of calcite on carboxylic acid functionalized self-assembled monolayer. *J. Am. Chem. Soc.* **125**, 4032-4033.
Hasse B., Ehrenberg H., Marxen J.C., Becker W. and Epple M. (2000) Calcium carbonate modifications in the mineralized shell of the freshwater snail Biomphalaria glabrata. *Chemistry – A European Journal* **6**, 3679-3685.
Hastings D.W., Emerson S.R. and Mix A.C. (1996) Vanadium in foraminiferal calcite as a tracer for changes in the areal extent of reducing sediments. *Paleoceanography* **11**, 665-678.
Hild S., Marti O. and Ziegler A. (2008) Spatial distribution of calcite and amorphous calcium carbonate in the cuticle of the terrestrial crustaceans Porcellio scaber and Armadillidium vulgare. *J. Struct. Biol.* **163**, 100-108.
Hu Q., Nielsen M.H., Freeman C.L., Hamm L.M., Tao J., Lee J.R.I., Han T.Y.J., Becker U., Harding J.H., Dove P.M. and Yoreo J.J.D. (2012) The thermodynamics of calcite nucleation: Classical vs. Non-classical pathways. *Faraday Discuss.* **159**, 509-523.
Ihli J., Kim Y.-Y., Noel E.H. and Meldrum F.C. (2013) The effect of additives on amorphous calcium carbonate (ACC): Janus behavior in solution and the solid state. *Adv. Funct. Mater.* **23**, 1575-1585.
Jacob D.E., Wirth R., Soldati A.L., Wehrmeister U. and Schreiber A. (2011) Amorphous calcium carbonate in the shells of adult Unionoida. *J. Struct. Biol.* **173**, 241-249.
Klein R.T., Lohmann K.C. and Thayer C.W. (1996) Sr/Ca and 13C/12C ratios in skeletal calcite of Mytilus trossulus: Covariation with metabolic rate, salinity, and carbon isotopic composition of seawater. *Geochim. Cosmochim. Acta* **60**, 4207-4221.
Langmuir C.H., Vocke Jr R.D., Hanson G.N. and Hart S.R. (1978) A general mixing equation with applications to Icelandic basalts. *Earth Planet. Sci. Lett.* **37**, 380-392.
Lea D.W., Mashiotta T.A. and Spero H.J. (1999) Controls on magnesium and strontium uptake in planktonic foraminifera determined by live culturing. *Geochim. Cosmochim. Acta* **63**, 2369-2379.
Lee J.R.I., Han T.Y.-J., Willey T.M., Wang D., Meulenberg R.W., Nilsson J., Dove P.M., Terminello L.J., van Buuren T. and De Yoreo J.J. (2007) Structural development of mercaptophenol self-assembled monolayers and the overlying mineral phase during templated CaCO3 crystallization from a transient amorphous film. *J. Am. Chem. Soc.* **129**, 10370-10381.

Li W., Chakraborty S., Beard B.L., Romanek C.S. and Johnson C.M. (2012) Magnesium isotope fractionation during precipitation of inorganic calcite under laboratory conditions. *Earth Planet. Sci. Lett.* **333–334**, 304-316.

Loste E., Wilson R.M., Seshadri R. and Meldrum F.C. (2003) The role of magnesium in stabilising amorphous calcium carbonate and controlling calcite morphologies. *J. Cryst. Growth* **254**, 206-218.

Luquet G. and Marin F. (2004) Biomineralisations in crustaceans: storage strategies. *C. R. Palevol* **3**, 515-534.

Nielsen M.H., Aloni S. and De Yoreo J.J. (2014) In situ TEM imaging of CaCO3 nucleation reveals coexistence of direct and indirect pathways. *Science* **345**, 1158-1162.

Nürnberg D., Bijma J. and Hemleben C. (1996) Assessing the reliability of magnesium in foraminiferal calcite as a proxy for water mass temperatures. *Geochim. Cosmochim. Acta* **60**, 803-814.

Paquette J. and Reeder R.J. (1995) Relationship between surface structure, growth mechanism, and trace element incorporation in calcite. *Geochim. Cosmochim. Acta* **59**, 735-749.

Politi Y., Metzler R.A., Abrecht M., Gilbert B., Wilt F.H., Sagi I., Addadi L., Weiner S. and Gilbert P.U.P.A. (2008) Transformation mechanism of amorphous calcium carbonate into calcite in sea urchin larval spicule. *Proc. Natl. Acad. Sci.* **105**, 17362-17366.

Pontoni D., Bolze J., Dingenouts N., Narayanan T. and Ballauff M. (2003) Crystallization of calcium carbonate observed in-situ by combined small- and wide-angle X-ray scattering. *J. Phys. Chem. B* **107**, 5123-5125.

Raz S., Weiner S. and Addadi L. (2000) Formation of high-magnesian calcites via an amorphous precursor phase: Possible biological implications. *Adv. Mater.* **12**, 38-42.

Reddy M.M. and Nancollas G.H. (1976) The crystallization of calcium carbonate: IV. The effect of magnesium, strontium and sulfate ions. *J. Cryst. Growth* **35**, 33-38.

Roer R. and Dillaman R. (1984) The structure and calcification of the crustacean cuticle. *Am. Zool.* **24**, 893-909.

Teng H.H., Dove P.M., Orme C.A. and De Yoreo J.J. (1998) Thermodynamics of calcite growth: Baseline for understanding biomineral formation. *Science* **282**, 724-727.

Tribovillard N., Algeo T.J., Lyons T. and Riboulleau A. (2006) Trace metals as paleoredox and paleoproductivity proxies: An update. *Chem. Geol.* **232**, 12-32.

Vollmer R. (1976) Rb-Sr and U-Th-Pb systematics of alkaline rocks: The alkaline rocks from Italy. *Geochim. Cosmochim. Acta* **40**, 283-295.

Wallace A.F., Wang D., Hamm L.M., Knoll A.H. and Dove P.M. (2012) Eukaryotic Skeletal Formation. In *Fundamentals of Geobiology* (eds. A.H. Knoll, D.E. Canfield and K.O. Konhauser). Wiley-Blackwell, Chichester. pp. 150-187.

Wang D., Hamm L.M., Giuffre A.J., Echigo T., Rimstidt J.D., De Yoreo J.J., Grotzinger J. and Dove P.M. (2012) Revisiting geochemical controls on patterns of carbonate deposition through the lens of multiple pathways to mineralization. *Faraday Discuss.* **159**, 371-386.

Wang D., Wallace A.F., De Yoreo J.J. and Dove P.M. (2009) Carboxylated molecules regulate magnesium content of amorphous calcium carbonates during calcification. *Proc. Natl. Acad. Sci.* **106**, 21511-21516.

Weiner S. and Addadi L. (2011) Crystallization pathways in biomineralization. *Annu. Rev. Mater. Res.* **41**, 21-40.

Weiner S. and Dove P.M. (2003) An overview of biomineralization processes and the problem of the vital effect. *Rev. Mineral. Geochem.* **54**, 1-29.

Wolf S.E., Leiterer J., Kappl M., Emmerling F. and Tremel W. (2008) Early homogenous amorphous precursor stages of calcium carbonate and subsequent crystal growth in levitated droplets. *J. Am. Chem. Soc.* **130**, 12342-12347.

Wombacher F., Eisenhauer A., Böhm F., Gussone N., Regenberg M., Dullo W.C. and Rüggeberg A. (2011) Magnesium stable isotope fractionation in marine biogenic calcite and aragonite. *Geochim. Cosmochim. Acta* **75**, 5797-5818.

Xu J., Yan C., Zhang F., Konishi H., Xu H. and Teng H.H. (2013) Testing the cation-hydration effect on the crystallization of Ca–Mg–CO3 systems. *Proc. Natl. Acad. Sci.* **110**, 17750-17755.

Yu J., Elderfield H. and Hönisch B. (2007) B/Ca in planktonic foraminifera as a proxy for surface seawater pH. *Paleoceanography* **22**, PA2202.

Zeebe R.E. (2005) Stable boron isotope fractionation between dissolved B(OH)3 and B(OH)4−. *Geochim. Cosmochim. Acta* **69**, 2753-2766.

Ziegler A. (1994) Ultrastructure and electron spectroscopic diffraction analysis of the sternal calcium deposits of Porcellio scaber Latr. (Isopoda, Crustacea). *J. Struct. Biol.* **112**, 110-116.

APPENDIX A. SUPPLEMENTARY INFORMATION FOR CHAPTER 1

A1. SIZE AND POLYDISPERSITY OF POLYSACCHARIDES

Dynamic light scattering (DLS) was used to estimate the average size (Z-ave) and polydispersity (PDI) of dissolved alginate and chitosan as a function of ionic strength. A suite of PS solutions were prepared using 1 g/L of sodium alginate (<50% guluronic acid, Novamatrix) or chitosan chloride (75-90% deacetylated, Novamatrix) at varying ionic strength (~0 mM to 600 mM) using sodium chloride (99.999%, Sigma-Aldrich). These ultrapure compounds contain less than 100 EU/gram of endotoxins. Due to the insolubility of chitosan above pH of 6, the pH of the solutions was not adjusted and was measured as 7.5±1.0 for alginate and 5.3±1.0 for chitosan solutions. Using a Malvern Zetasizer NanoZS, samples were placed in disposable cuvettes and the temperature of each sample was equilibrated to 25°C for 2 min. A total of 6 measurements of scattered light intensity were collected for each PS and ionic strength condition, with 13-17 replicates per measurement. The data were automatically compiled and processed following ISO standard document 13321: 1996 E and ISO 22412:2008 using Malvern software by a cumulants analysis fit to the autocorrelation function of scattered light to obtain estimates of size (Z-ave) and dispersion in size (polydispersity index, PDI).

Intensity scattering estimates for PS diameter (Z-ave) show a steady decrease in size with increasing IS up to 100 mM, above which there is no significant dependence (**Fig. A.1**). The decreasing trend in Z-ave with ionic strength supports the idea for coiling due to charge screening. On the other hand, the Z-ave measurements at high ionic strength are slightly larger than predicted values. From the molecular weight range provided by the supplier, the expected diameter for chitosan is 89-154 nm and for alginate is 61-105 nm (purple and red shaded regions in **Fig. A.1A**). These are calculated

from the relationship between radius of gyration and molecular weight (Rinaudo, 2006). The behavior at low ionic strength may be explained by interpreting the uniformity of dispersion in sizes through the polysdispersity index, or PDI (**Fig. A.1B**). Samples with large PDI values are polydisperse and they produce a larger error in calculations of Z-ave by this technique. This calls into question the quality of measurements for Z-ave below ionic strengths of 100 mM NaCl. The relatively low PDI above 100 mM NaCl may be evidence for aggregation occurring in this range to create a uniform size distribution.

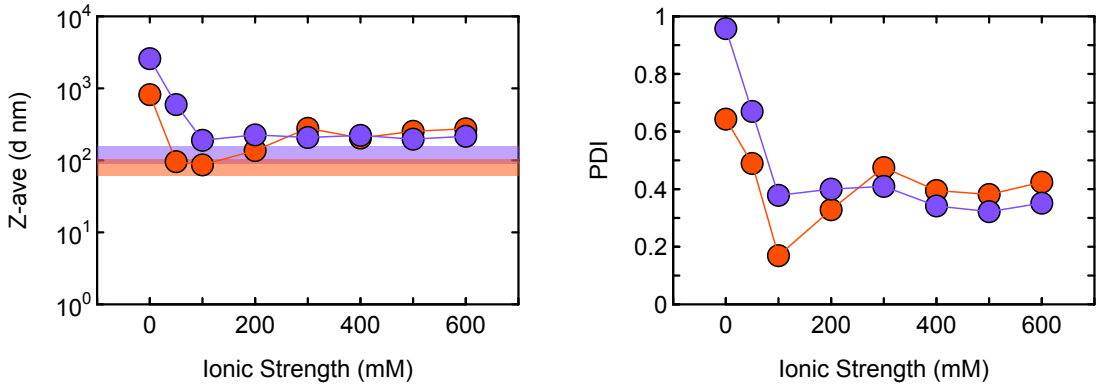

Fig. A.1: Measurements of alginate alginate (red) and chitosan (purple) as a function of ionic strength using dynamic light scattering show a decreasing trend in PS diameter (Z-ave) and PS dispersion in size (PDI). A) The decrease in Z-ave is consistent with aggregation and/or PS coiling. The measured values are slightly greater than expected values for diameter from radius of gyration calculations. B) However, the polydispersity index at ionic strength <100 mM is large, suggesting a large size distribution. The low PDI and uniform dispersion at high ionic strengths may be indicative of aggregation.

Table A.1: PS diameter (Z-ave) and PS dispersion in size (PDI) are shown for alginate and chitosan as a function of ionic strength. Data are shown in **Fig. A.1**.

	Alginate		Chitosan	
Ionic Strength (mM)	Z-ave (d nm)	PDI	Z-ave (d nm)	PDI
0	818.1	0.6432	2585	0.9575
50	95.86	0.4893	595.1	0.6698
100	86.49	0.1690	190.0	0.3875
200	136.8	0.3285	225.9	0.4002
300	278.5	0.4750	207.9	0.4095
400	204.3	0.3953	222.2	0.3417
500	253.4	0.3815	196.9	0.3218
600	274.4	0.4242	216.1	0.3513

A2. ELECTROPHORETIC MOBILITY AND ZETA POTENTIAL OF PS

The electrophoretic mobility of dissolved alginate and chitosan was measured to estimate the change in PS charge as a function of ionic strength from 0 mM to 600 mM. Using the same solution preparation described in **Appendix A1**, the measurements were conducted at 25°C in disposable capillary cells (Malvern DTS1070) on the Malvern Zetasizer NanoZS. Each sample was measured 4 times with 40 replicates averaged for each measurement. Zeta potential was calculated from electrophoretic mobility measurements using the Helmhotz-Smoluchowski equation and assuming a viscosity of 0.8872 cP, refractive index of 1.330, and dielectric constant of 78.5 (Delgado et al., 2007).

The amount of charge on the chitosan and alginate molecules was also characterized as a function of ionic strength by measuring particle mobility in an electric field. The electrophoretic mobility was then used to estimate the zeta potential (**Fig. A.2**). As expected, chitosan was positively charged and alginate was negatively charged. These charges decrease in magnitude with increasing ionic strength, a trend that supports greater charge screening and/or aggregation at high ionic strengths. Furthermore, these measurements are convoluted with the particle size analysis by DLS, where low ionic strength conditions with a non-uniform dispersion in size hamper the reliability of measuring electrophoretic mobility.

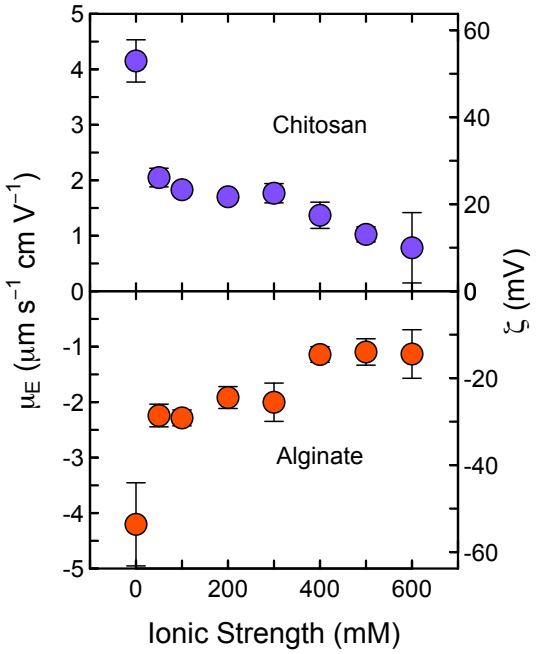

Fig. A.2: Electrophoretic mobility measurements and zeta potential calculations for chitosan (purple) and alginate (red) show trends that indicate the mobility and charge of PS decreases in higher ionic strength solutions.These measurements may reflect charge screening due to coiling and/or aggregation of PS with increasing ionic strength.

Table A.2: Measurements of PS electrophoretic mobility, μ_E, and calculated zeta potential, ζ, are shown for alginate and chitosan as a function of ionic strength. Data are shown in **Fig. A.2**.

	Alginate			Chitosan		
Ionic Strength (mM)	μ_E (μm s^{-1} cm V^{-1})	error	ζ (mV)	μ_E (μm s^{-1} cm V^{-1})	error	ζ (mV)
0	-4.203	±0.749	-53.6	4.152	±0.381	53.0
50	-2.241	±0.204	-28.6	2.049	±0.169	26.4
100	-2.284	±0.143	-29.1	1.830	±0.067	23.7
200	-1.917	±0.197	-24.4	1.703	±0.096	22.5
300	-2.002	±0.345	-25.5	1.766	±0.174	23.8
400	-1.141	±0.141	-14.6	1.369	±0.237	17.5
500	-1.096	±0.238	-14.0	1.024	±0.136	13.1
600	-1.133	±0.438	-14.5	0.7827	±0.634	9.99

A3. POTENTIOMETRIC TITRATION OF PS

Potentiometric titrations of 0.2 g/L solutions of alginate and chitosan (same materials as in **Appendix A2**) were made at solution ionic strengths varying from ~0 mM to 600 mM to estimate changes in protonation of functional groups on PS with ionic strength. The measurements were conducted using Metrohm 836 Titrando equipped with

a Metrohm 800 Dosino. To ensure complete deprotonation of alginate carboxyl groups before the titration began, 2 mL 0.01 N NaOH (Metrohm) was added to the solution. Likewise, 1 mL of 0.01 N HCl (Metrohm) was added to ensure protonation of chitosan amine groups. Appropriate volumes of NaCl stock solution was added to achieve ionic strength varying from ~0 mM to 600 mM and the total volume was diluted to 50 mL. The solutions were gently bubbled with moistened N_2 gas (achieved by first bubbling gas through DI water) for 1 hour to remove CO_2 from the system. Titrations were conducted under stirring and N_2 bubbling in a closed double walled glass vessel at 25°C using a pH electrode that was calibrated daily. PS solutions were titrated using commercially assayed solutions of 0.01 N NaOH or 0.01 HCl (Metrohm) and solution pH was recorded as a function of volume of titrant added (**Fig. A.3**).

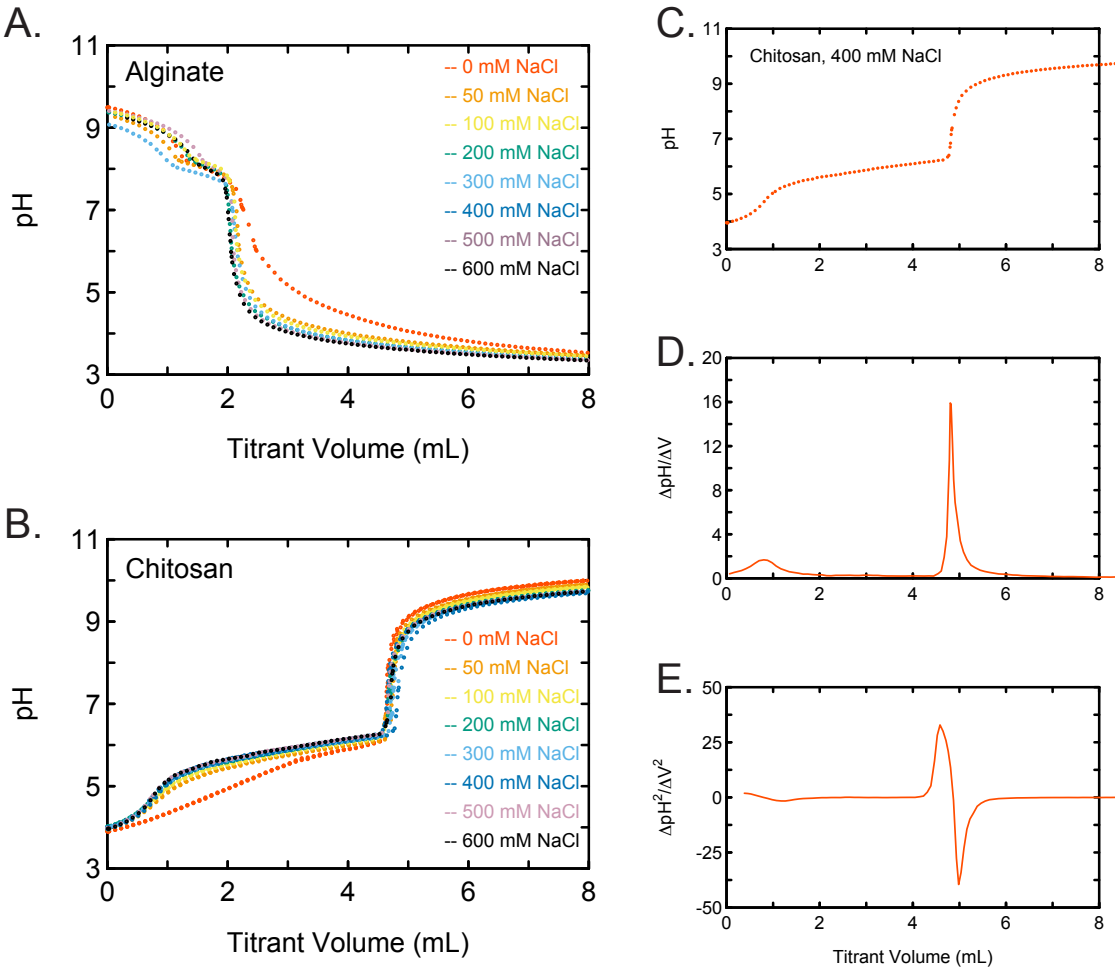

Fig. A.3: Potentiometric titration curves for A) alginate and B) chitosan at varying ionic strength from ~0 to 600 mM. The first equivalence point in the curves corresponds to titration of excess acid or base added. Equivalence points were determined by manually calculating the derivative of the titration curves. One example is displayed in C-E of C) titration of chitosan at 400 mM NaCl and its D) first and E) second derivative plots.

Experiments for chitosan were conducted in triplicate. The titration curves show two equivalence points: the first reflects neutralization of the excess acid or base added, while the second corresponds to deprotonation of NH_3^+ (Balázs et al., 2007). These equivalence points were estimated from 1st and 2nd derivative plots of the titration curves (**Fig. A.3**). The number of protonated amine groups on chitosan were calculated from the volume of titrant between the two equivalence points on the titration curves. The calculated number of charged NH_3^+ groups on chitosan appear to have no dependence on

ionic strength (**Fig. A.4**). A similar analysis was performed to estimate the number of deprotonated COO^- groups on alginate. The number of unprotonated COO^- groups on alginate appear to have no definitive relationship to solution ionic strength (**Fig. A.4**).

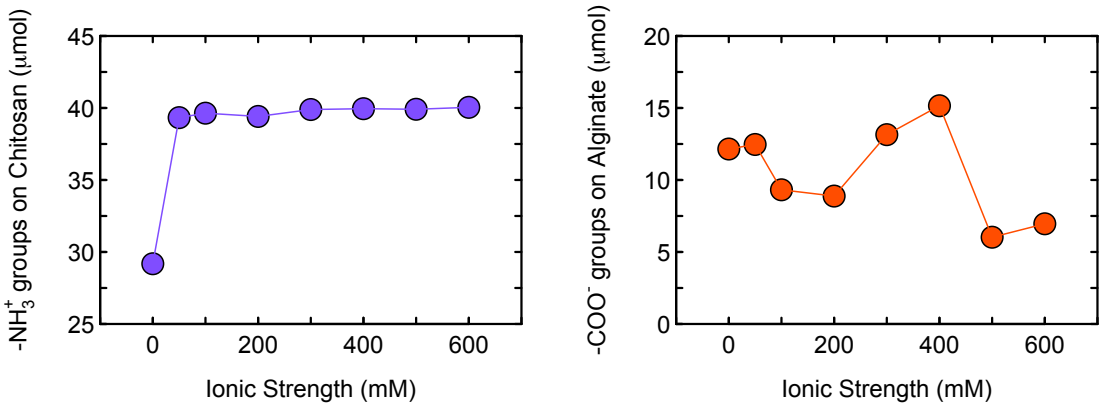

Fig. A.4: Potentiometric titrations of chitosan and alginate have no apparent trend in calculated number of charged groups with varying ionic strength. A) The number of protonated amine groups of chitosan suggest protonation and charge is independent of ionic strength. B) The estimated number of deprotonated carboxyl groups of alginate have no clear relationship with changing ionic strength conditions.

A4. EFFECT OF IONIC STRENGTH ON HETEROGENEOUS NUCLEATION

Measurements of calcite nucleation rates onto alginate and chitosan substrates show the expected linear behavior between ln J_0 and $1/\sigma^2$ from CNT (**Eq. 1.4**). As seen in **Fig. A.5**, the data show faster nucleation rates at higher supersaturation (left side of plot) and under higher ionic strength conditions. As shown in previous studies, the nucleation rates are uniquely dependent upon the substrate functional group chemistry (alginate vs chitosan) producing different trends in slope, B, which serves as a proxy for the energy barrier to nucleation, ΔG (**Eq. 1.3**) (Hu et al., 2012; Giuffre et al., 2013; Hamm et al., 2014). In other words, at a given solution ionic strength, alginate has a higher energy barrier than chitosan. This is consistent with previous findings (Giuffre et al., 2013), where the smaller nucleation barriers on chitosan are attributed to its low

charge density and low hydrophilicity that are more energetically favorable to form an interface with calcite by reducing substrate-liquid interfacial area.

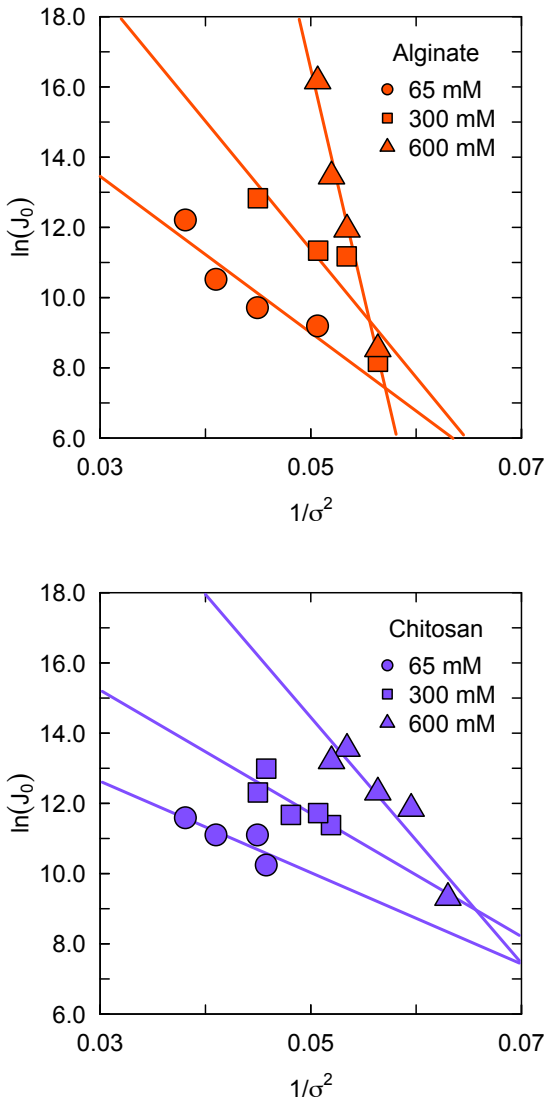

Fig. A.5: Linearized function of heterogeneous nucleation rates of calcite onto two polysaccharide substrates: A) alginate and B) chitosan. Both polysaccharides show an increase in slope of this linear dependence at higher ionic strength conditions. The rate values are tabulated in **Table A.3**.

By correlating B with solution ionic strength (**Fig. A.6**), we show the energy barriers to nucleation on alginate and chitosan are higher with increasing ionic strength. Furthermore, the increase in nucleation barriers for alginate is much more extreme. To

further understand these trends, we characterized physical and chemical properties of PS such as conformation of functional groups, charge, and speciation as a function of ionic strength.

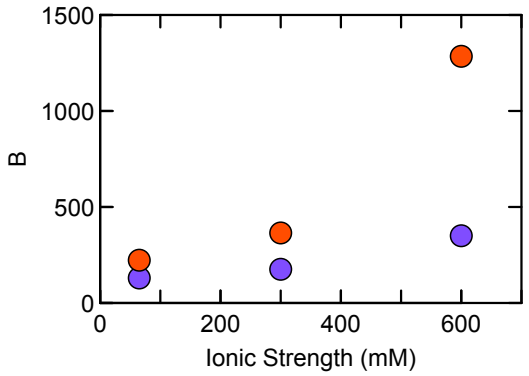

Fig. A.6: Energy barriers to nucleation, B, are greater with increasing ionic strength for both alginate (red) and chitosan (purple). Values for B are calculated using **Eq. 1.3** from the slopes of trends in **Fig. A.5** and tabulated in **Table A.5**.

Table A.3: Summary of solution compositions and supersaturation used in nucleation experiments onto alginate and chitosan at varying ionic strength. Solution ionic strength, activity of Ca^{2+} and activity of CO_3^{2-} are modeled by Geochemist's Workbench from initial [$CaCl_2$], [$NaHCO_3$], and [NaCl] at pH of 8.50 and temperature of 298 K. Supersaturation values are calculated according to the expression, $\sigma = \ln\left(\frac{a_{Ca^{2+}} a_{CO_3^{2-}}}{K_{sp,calcite}}\right)$.

[$CaCl_2$] (mM)	[$NaHCO_3$] (mM)	[NaCl] (mM)	Ionic Strength (mM)	log a_{Ca}	log a_{CO3}	σ
2.000	50.0	0	53.1	-3.2755	-3.2746	4.44
2.410	56.9	0	60.4	-3.2250	-3.2250	4.67
2.500	58.4	0	62.0	-3.2156	-3.2156	4.72
3.000	66.3	0	70.4	-3.1674	-3.1677	4.94
3.500	73.8	0	78.3	-3.1272	-3.1276	5.12
2.870	58.3	244	300.0	-3.3252	-3.3257	4.21
3.080	61.8	241	300.5	-3.3001	-3.3007	4.33
3.200	63.8	239	300.5	-3.2869	-3.2866	4.39
3.300	65.5	237	300.2	-3.2755	-3.2757	4.44
3.550	69.5	233	300.2	-3.2499	-3.2500	4.56
3.815	73.7	229	300.5	-3.2247	-3.2250	4.67
3.910	75.2	227	300.0	-3.2159	-3.2163	4.72
3.325	61.5	544	600.1	-3.3750	-3.3754	3.98
3.550	65.2	541	600.6	-3.3503	-3.3502	4.10
3.790	69.1	537	600.2	-3.3257	-3.3250	4.21
4.050	73.1	533	599.9	-3.3007	-3.3006	4.33
4.200	75.3	531	599.9	-3.2871	-3.2878	4.39
4.340	77.5	529	600.0	-3.2750	-3.2753	4.44

Table A.4: Nucleation rates of calcite onto alginate and chitosan at varying ionic strength. Rates are normalized to 1.23 mm^2 viewing area of optical microscope. Data are also presented in **Fig. A.5**.

		Alginate, IS 65 mM		Alginate, IS 300 mM		Alginate, IS 600 mM	
σ	$1/\sigma^2$	J_0 (m^{-2} s^{-1})	$\ln(J_0)$	J_0 (m^{-2} s^{-1})	$\ln(J_0)$	J_0 (m^{-2} s^{-1})	$\ln(J_0)$
4.21	0.0564	---	---	3542	8.17	5095	8.54
4.33	0.0534	---	---	71265	11.17	153592	11.94
4.39	0.0520	---	---	---	---	697584	13.46
4.44	0.0507	9838	9.19	83886	11.34	10478001	16.16
4.72	0.0450	16539	9.71	373120	12.83	---	---
4.94	0.0410	37098	10.52	---	---	---	---
5.12	0.0381	201074	12.21	---	---	---	---
		Chitosan, IS 65 mM		Chitosan, IS 300 mM		Chitosan, IS 600 mM	
σ	$1/\sigma^2$	J_0 (m^{-2} s^{-1})	$\ln(J_0)$	J_0 (m^{-2} s^{-1})	$\ln(J_0)$	J_0 (m^{-2} s^{-1})	$\ln(J_0)$
3.98	0.0630	---	---	---	---	11080	9.31
4.10	0.0595	---	---	---	---	140019	11.85
4.21	0.0564	---	---	---	---	222742	12.31
4.33	0.0534	---	---	---	---	773053	13.56
4.39	0.0520	---	---	87663	11.38	543579	13.21
4.44	0.0507	---	---	123413	11.72	---	---
4.56	0.0481	---	---	117199	11.67	---	---
4.67	0.0458	28140	10.24	437614	12.99	---	---
4.72	0.0449	66279	11.10	222006	12.31	---	---
4.94	0.0410	66364	11.10	---	---	---	---
5.12	0.0381	108158	11.59	---	---	---	---

Table A.5: Proxy for the thermodynamic barrier to nucleation, B, is derived from slopes of linear trends in **Fig. A.5** and from data in **Table A.4**. Errors in B are calculated from $\pm 1\sigma$ standard error of linear regression through data in **Table A.4**. Values for γ_{net} are calculated from **Eq. B.4** assuming F of $16\pi/3$, ω of 6.13×10^{-29} m^3/molecule, and T of 298±1 K.

	Ionic Strength (mM)	B	error in B	γ_{net} (mJ/m^2)
Alginate	65	223	±20	62.7
	300	364	±30	73.9
	600	1284	±81	112.5
Chitosan	65	130	±17	52.4
	300	175	±20	57.9
	600	350	±32	72.9

A5. EFFECT OF IONIC STRENGTH ON HOMOGENEOUS NUCLEATION

Homogeneous nucleation experiments were performed in a closed glass vessel under 300 rpm stirring at constant temperature of 25±1°C. Two 50 mL solutions of

$CaCl_2$±NaCl and $NaHCO_3$±NaCl were mixed inside the closed glass vessel. The induction time to calcite nucleation was measured by *in situ* monitoring of the simultaneous decrease in pH and $[Ca^{2+}]$ using two electrodes. The pH electrode was calibrated daily using 4.01, 7.00, and 10.01 standards. The Ca ion selective electrode was cleaned and the KCl/Ag/AgCl filling solution was replaced daily, typically every 3 to 4 experiments. This electrode was also calibrated daily using new standard $CaCl_2$ solutions with NaCl added to achieve the same ionic strength as the experimental conditions. All electrodes, electrode filling solutions, and calibration standards were purchased from Thermo Scientific Orion.

Two electrodes monitored solution pH and $[Ca^{2+}]$ every 5 seconds for the duration of each experiment (**Fig. A.7**). Upon mixing, the solution pH stabilized (i.e. constant over a 5 second interval) after ~45 seconds while $[Ca^{2+}]$ stabilized after 3-4 minutes. The electrode readings experienced either positive or negative drift with no consistent behavior across replicates for experiments and no correlation to solution conditions. However, for experiments with induction times >40 minutes, the drift in pH was often positive and the drift in $[Ca^{2+}]$ was negative, which agreed in direction and magnitude with drift in long duration readings (>1 hour) of the standard solutions. As shown in **Fig. A.7**, a linear regression was fit to the drift of each experiment between the time of the first stable reading and the time of rapid decrease in the reading. The induction time was thus determined to be the time of deviation of pH and $[Ca^{2+}]$ measurements from this linear fit, with good agreement between the two electrodes (<30 seconds).

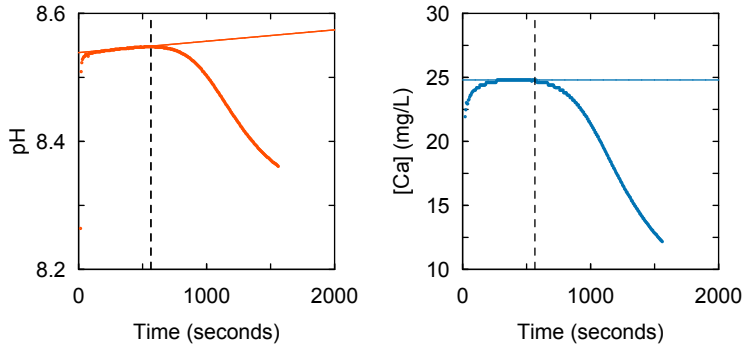

Fig. A.7: Example of measurements of pH and [Ca^{2+}] in a homogeneous nucleation experiment. Drift in measurements over time was fit to data. Induction time was defined as the moment the data deviate from drift.

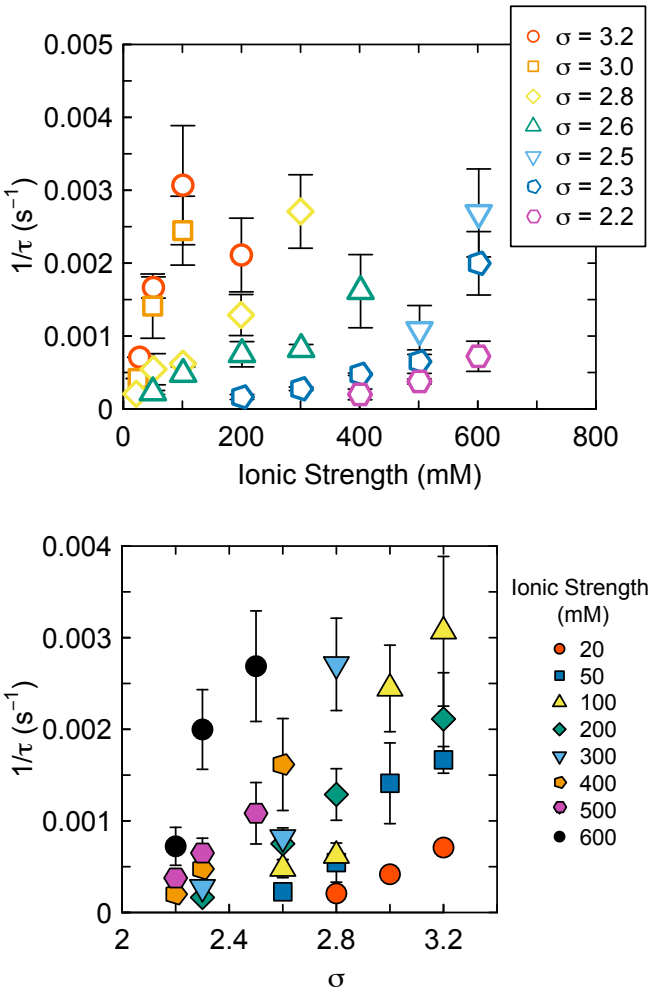

Fig. A.8: Homogeneous nucleation experiments show a decrease in induction time with higher supersaturation and higher ionic strength. The inverse of induction time is correlated to A) ionic strength at varying supersaturations and B) supersaturation at varying ionic strengths. Error bars represent standard deviation from three replicate experiments. Rate measurements are summarized in **Table A.6**.

Table A.6: Induction time to homogeneous nucleation is shown as a function of ionic strength and supersaturation with respect to calcite. Data are also presented in **Fig. A.8**.

Ionic Strength (mM)	σ	$1/\tau$ (s^{-1})	error
20	2.8	0.000208	--
	3.0	0.000418	--
	3.2	0.000709	--
50	2.6	0.000226	±0.000028
	2.8	0.000545	±0.000214
	3.0	0.001410	±0.000441
	3.2	0.001666	±0.000146
100	2.6	0.000479	±0.000099
	2.8	0.000621	±0.000026
	3.0	0.002446	±0.000472
	3.2	0.003070	±0.000817
200	2.3	0.000164	±0.000034
	2.6	0.000750	±0.000173
	2.8	0.001288	±0.000282
	3.2	0.002112	±0.000505
300	2.3	0.000276	±0.000024
	2.6	0.000820	±0.000064
	2.8	0.002709	±0.000504
400	2.2	0.000200	±0.000073
	2.3	0.000475	±0.000016
	2.6	0.001615	±0.000502
500	2.2	0.000377	±0.000034
	2.3	0.000649	±0.000162
	2.5	0.001083	±0.000335
600	2.2	0.000722	±0.000207
	2.3	0.001998	±0.000435
	2.5	0.002689	±0.000603

A6. REFERENCES

Balázs N. and Sipos P. (2007) Limitations of pH-potentiometric titration for the determination of the degree of deacetylation of chitosan. *Carbohydr. Res.* **342**, 124-130.

Delgado A.V., González-Caballero F., Hunter R.J., Koopal L.K. and Lyklema J. (2007) Measurement and interpretation of electrokinetic phenomena. *J. Colloid Interface Sci.* **309**, 194-224.

Giuffre A.J., Hamm L.M., Han N., De Yoreo J.J. and Dove P.M. (2013) Polysaccharide chemistry regulates kinetics of calcite nucleation through competition of interfacial energies. *Proc. Natl. Acad. Sci.* **110**, 9261-9266.

Hamm L.M., Giuffre A.J., Han N., Tao J., Wang D., De Yoreo J.J. and Dove P.M. (2014) Reconciling disparate views of template-directed nucleation through measurement of calcite nucleation kinetics and binding energies. *Proc. Natl. Acad. Sci.* **111**, 1304-1309.

Hu Q., Nielsen M.H., Freeman C.L., Hamm L.M., Tao J., Lee J.R.I., Han T.Y.J., Becker U., Harding J.H., Dove P.M. and Yoreo J.J.D. (2012) The thermodynamics of calcite nucleation: Classical vs. Non-classical pathways. *Faraday Discuss.* **159**, 509-523.

Rinaudo M. (2006) Chitin and chitosan: properties and applications. *Prog. Polym. Sci.* **31**, 603-632.

APPENDIX B. SUPPLEMENTARY INFORMATION FOR CHAPTER 2

B1. MEASUREMENTS OF SURFACE FREE ENERGY

The $\gamma_{S\text{-air}}$ measurements were conducted using a well-established method by Owens, Wendt, Rabel, and Kaelble (OWRK) (Owens et al., 1969; Kaelble, 1970; Rabel, 1971). Static contact angle, θ, was measured with a goniometer on electrodeposited PS substrates using three test liquids: 18.2 MΩ deionized water, glycerol (Fisher, 99.5%), and ethylene glycol (Aldrich, 99.7%) with known polar and dispersive components to surface free energy (γ_L^p and γ_L^d). Six angle measurements (three left and three right) were made on three replicate droplets of each test liquid. The mean angle θ as a function of γ_L^p/γ_L^d was measured according to the following expression

$$\frac{\gamma_L(\cos\theta+1)}{2\sqrt{\gamma_L^d}} = \sqrt{\gamma_S^d} + \sqrt{\gamma_S^p}\left(\frac{\sqrt{\gamma_L^p}}{\sqrt{\gamma_L^d}}\right) \qquad [B.1]$$

where γ_L is the sum of γ_L^p and γ_L^d and with two parameters γ_S^p and γ_S^d that correspond to polar and dispersive components to surface tension of the substrate. Contact angles are linearly related to a function of γ_L, γ_L^p, and γ_L^d according to the above expression where $\sqrt{\gamma_S^d}$ and $\sqrt{\gamma_S^p}$ correspond to the intercept and slope, respectively as seen in **Fig. B1**. The $\gamma_{S\text{-}air}$ for each polysaccharide substrate is given by the sum of γ_S^p and γ_S^d. The results from the OWRK method are presented in **Table B.1**.

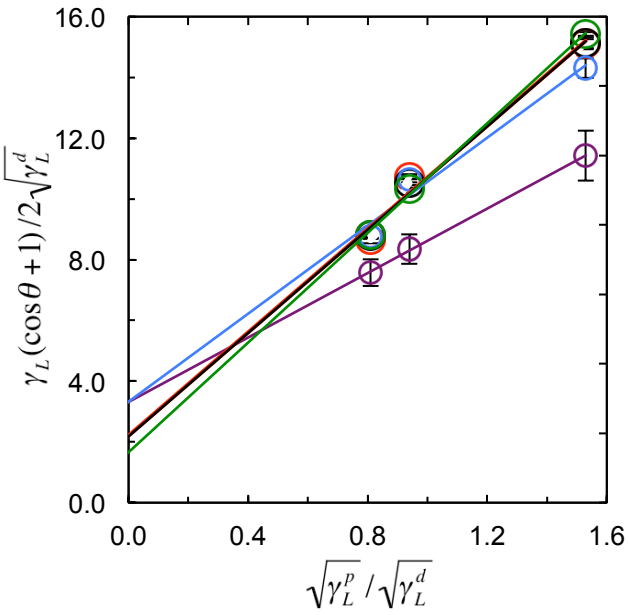

Fig. B.1: Contact angle measurements determine the surface free energy in air (gS-air) of polysaccharide substrates by the relationship in **Eq. (A9)**. The intercept $\sqrt{\gamma_S^d}$ corresponds to dispersive contribution of $\gamma_{S\text{-}air}$ and the slope $\sqrt{\gamma_S^p}$ corresponds to its polar contribution. Errors are calculated from the standard deviation of contact angle measurements. Heparin in green, LG alginate in red, HG alginate in black, hyaluronate in blue, and chitosan in purple.

Table B.1: Summary of surface free energy and its polar and dispersive components from OWRK calculations.

	γ_S^p (mJ/m^2)	γ_S^d (mJ/ m^2)	$\gamma_{S\text{-}air}$ (mJ/ m^2)
Chitosan	28.1	11.0	39.1
Hyaluronate	52.4	11.1	63.5
HG Alginate	72.3	4.77	77.1
LG Alginate	72.2	4.88	77.1
Heparin	81.4	2.76	84.2

B2. CLASSICAL NUCLEATION THEORY

Classical nucleation theory (Nielsen, 1964; Chernov, 1984) states that the flux of new nuclei onto a substrate is given by

$$J_o = A\exp\left(\frac{-\Delta G^*}{k_B T}\right) \qquad [B.2]$$

where J_o is the steady state rate of heterogeneous nucleation (m^{-2} s^{-1}), ΔG^* is the free energy barrier to forming critical nuclei, k_B is the Boltzmann constant, and T is temperature. The pre-exponential factor, A, is dependent upon kinetic factors that include rates of ion desolvation, attachment, and detachment. Expanding ΔG^* in **Eq. (B.2)** yields

$$\Delta G^* = \frac{F\omega^2\gamma_{net}^3}{k_B T\sigma^2} \qquad [B.3]$$

and

$$J_o = A\exp\left(\frac{-F\omega^2\gamma_{net}^3}{k_B^2 T^2\sigma^2}\right) \qquad [B.4]$$

where F is a nucleus shape factor, ω is molecular volume of calcite, and γ_{net} is the net surface free energy of the crystal-substrate-liquid system (mJ m^{-2}). Assuming that ω is relatively constant, the experimental variables within ΔG^* are σ and γ_{net} for a constant T.

That is, the thermodynamic barrier to nucleation has two major energetic contributions: supersaturation, which is a function of chemical potential, and the surface free energy of the system. To evaluate the influence of these terms on the nucleation rate, we define

$B = \frac{F\omega^2\gamma_{net}^3}{k_B^3 T^3}$ so that **Eq. (B.4)** becomes

$$J_o = A\exp\left(\frac{-B}{\sigma^2}\right) \qquad \text{[B.5].}$$

Transforming **Eq. (B.5)** into a linear form:

$$\ln(J_o) = \ln(A) - \frac{B}{\sigma^2} \qquad \text{[B.6].}$$

The slope of this relationship, B, serves as a proxy for the energy barrier to nucleation. This can be seen by comparing **Eq. (B.3)** and **Eq. (B.5)** to explicitly show the dependence of the energy barrier to nucleation on B and σ:

$$\Delta G^* = \frac{Bk_B T}{\sigma^2} \qquad \text{[B.7]}$$

Thus, B represents the surface energy contribution of ΔG^* at any given σ. Because γ_{net} is always positive, B is also always positive and large values of B will always correspond to large ΔG^* for all supersaturations.

B3. CALCULATION OF CHARGE FROM ACID DISSOCIATION CONSTANTS

Net charge of the polysaccharide substrates was estimated by using the solution pH and published acid dissociation constants (pK_a) of functional groups on organic acids and bases (Lide, 2012). The ratio (R) of activities of a deprotonated species (a_X) to its protonated form (a_{HX}) can be calculated using a modification of the Henderson-Hasselbach equation

$$pH = pK_a + \log\left(\frac{a_X}{a_{HX}}\right) \qquad [B.8]$$

$$R = \left(\frac{a_X}{a_{HX}}\right) = 10 \wedge (pH - pK_a) \qquad [B.9]$$

The average amount of charge (Z) per functional group at a given pH is defined as the proportion of charged species to total number of species. For functional groups that are negatively charged when deprotonated, the relative contribution of charge can be calculated from R by the relation:

$$Z_A = \frac{a_{A^-}}{a_{A^-} + a_{HA}} = \frac{-R}{R+1}\,. \qquad [B.10]$$

For functional groups that are positively charged when protonated, the charge is calculated from R according to

$$Z_B = \frac{a_{HB^+}}{a_B + a_{HB^+}} = \frac{1}{R+1}\,. \qquad [B.11]$$

The total charge per monosaccharide (Z_{tot}) is then calculated by adding the relative contribution of Z from each functional group (See **Table B.2**).

Table B.2: Estimates of charge using acid dissociation constants of organic acids that represent different functional groups on the polysaccharide. The number of functional groups per monosaccharide (MS) was determined from the reported chemical characterizations by the vendor. Final total charge is reported as charge per monosaccharide.

Polysaccharide	Representative Organic Acid	pK_a	R	Z	Number of Groups per MS	Charge (Z_{tot}) per MS
Heparin	Glucose-OH	12.46	2.18×10^{-2}	-0.02	1*	
	Cyclohexane carboxylic acid	4.91	7.76×10^{6}	-1.00	0.5	
	Acetamide	15.1	5.01×10^{-5}	0.00	0.1	
	Isopropylamine	10.63	1.48×10^{0}	0.40	0.4	
	Sulfuric acid	1.99	1.26×10^{10}	-1.00	1	-1.36
Alginate	Glucose-OH	12.46	2.18×10^{-2}	-0.02	1*	
	Cyclohexane carboxylic acid	4.91	7.76×10^{6}	-1.00	1	-1.02
Hyaluronate	Glucose-OH	12.46	2.18×10^{-2}	-0.02	1*	
	Cyclohexane carboxylic acid	4.91	7.76×10^{6}	-1.00	0.5	
	Acetamide	15.1	5.01×10^{-5}	0.00	0.5	-0.52
Chitosan	Glucose-OH	12.46	2.18×10^{-2}	-0.02	1*	
	Acetamide	15.1	5.01×10^{-5}	0.00	0.25	
	Isopropylamine	10.63	1.48	0.40	0.75	0.28

*For each monosaccharide ring, only one hydroxyl group was assumed to be acidic.

B4. CALCULATION OF CHARGE DENSITY OF SAM AND PS SUBSTRATES

The charge density of the Au(111) SAMs used in Hu et al. (2012) was estimated by assuming that the head group spacing was a constant value of 4.97 Å (Li et al., 1995; Aizenberg et al., 1999; Mendoza et al., 2007). The hexagonal packing predicts a density

of 4.67 head groups/nm^2, which was scaled to charge according to pK_a values for SAMs of different functional group chemistry.

To estimate the charge density of the polysaccharide substrates, we assumed the films have a surface density of functional groups that is similar to crystalline a-chitin, which has a monosaccharide density of 2.28 units/nm^2 (Rinaudo, 2006). The calculated values represent an upper limit to charge density because electrodeposited PS substrates are most likely less ordered with a lower functional group density than crystalline a-chitin. Charge was estimated according to pK_a values of all functional groups within the polysaccharide chain.

B5. ADDITIONAL TABLES OF DATA

Table B.3: Summary of solution compositions and supersaturation used in nucleation experiments onto PS substrates. Activity of Ca^{2+} and CO_3^{2-} are modeled by Geochemist's Workbench from initial solution composition and initial pH. Supersaturation with respect to calcite is calculated from a_{Ca} and a_{CO3} according to **Eq. 2.1**.

$[CaCl_2]$ (mM)	$[Na_2CO_3]$ (mM)	pH	log a_{Ca}	log a_{CO3}	σ
1.75	1.75	10.796	-3.1408	-3.2436	4.83
2.00	2.00	10.812	-3.1043	-3.2026	5.00
2.25	2.25	10.837	-3.0732	-3.1656	5.16
2.50	2.50	10.813	-3.0426	-3.1393	5.29
2.75	2.75	10.877	-3.0208	-3.1044	5.42
3.00	3.00	10.856	-2.9960	-3.0830	5.53
3.25	3.25	10.844	-2.9738	-3.0626	5.63

Table B.4: Nucleation rates of calcite onto PS substrates in 1.23 mm^2 viewing area of optical microscope over the course of experiment. Data are shown in **Fig. 2.2**.

		Heparin		LG Alginate		HG Alginate	
σ	$1/\sigma^2$	J_0 (m^{-2} s^{-1})	$\ln(J_0)$	J_0 (m^{-2} s^{-1})	$\ln(J_0)$	J_0 (m^{-2} s^{-1})	$\ln(J_0)$
4.83	0.0429	---	---	---	---	7770	8.96
5.00	0.0399	59587	11.00	---	---	---	---
5.16	0.0375	119383	11.69	38366	10.55	62944	11.05
5.29	0.0357	123306	11.72	75941	11.24	88124	11.39
5.42	0.0340	427959	12.97	152208	11.93	165452	12.02
5.53	0.0327	547153	13.21	---	---	125108	11.74
5.63	0.0316	1690726	14.34	---	---	---	---

		Hyaluronate		Chitosan	
σ	$1/\sigma^2$	J_0 (m^{-2} s^{-1})	$\ln(J_0)$	J_0 (m^{-2} s^{-1})	$\ln(J_0)$
4.83	0.0429	---	---	---	---
5.00	0.0399	---	---	28904	10.27
5.16	0.0375	---	---	53453	10.89
5.29	0.0357	140758	11.85	71067	11.17
5.42	0.0340	298258	12.61	71146	11.17
5.53	0.0327	342059	12.74	91906	11.43
5.63	0.0316	411923	12.93	28904	10.27

Table B.5: Proxy for the thermodynamic barrier to nucleation, B, is derived from slopes of linear trends in **Fig. 2.2** and from data in **Table B.4**. Errors in B are calculated from $\pm 1\sigma$ standard error of linear regression through data in **Table B.4**. Values for γ_{net} are calculated from **Eq. B.4** assuming F of $16\pi/3$, ω of 6.13×10^{-29} m^3/molecule, and T of 298±1 K. All experiments were conducted at a pH of 10.8 and ionic strength of ~10 mM.

	B	error in B	γ_{net} (mJ/m^2)
Heparin	376	60	74.7
LG Alginate	390	11	75.6
HG Alginate	294	45	68.8
Hyaluronate	253	58	65.4
Chitosan	121	22	51.2

B6. REFERENCES

Aizenberg J., Black A.J. and Whitesides G.M. (1999) Control of crystal nucleation by patterned self-assembled monolayers. *Nature* **398**, 495-498.

Chernov A.A. (1984) *Modern Crystallography III - Crystal Growth*. Springer-Verlag, Berlin.

Hu Q., Nielsen M.H., Freeman C.L., Hamm L.M., Tao J., Lee J.R.I., Han T.Y.J., Becker U., Harding J.H., Dove P.M. and Yoreo J.J.D. (2012) The thermodynamics of calcite nucleation: Classical vs. Non-classical pathways. *Faraday Discuss.* **159**, 509-523.

Kaelble D.H. (1970) Dispersion-polar surface tension properties of organic solids. *The Journal of Adhesion* **2**, 66-81.

Li J., Liang K.S., Scoles G. and Ulman A. (1995) Counterion Overlayers at the Interface between an Electrolyte and an .omega.-Functionalized Monolayer Self-Assembled on Gold. An X-ray Reflectivity Study. *Langmuir* **11**, 4418-4427.

Lide D.R. (2012) *CRC Handbook of Chemistry and Physics*. CRC Press.

Mendoza S.M., Arfaoui I., Zanarini S., Paolucci F. and Rudolf P. (2007) Improvements in the characterization of the crystalline structure of acid-terminated alkanethiol self-assembled monolayers on Au(111). *Langmuir* **23**, 582-588.

Nielsen A.E. (1964) *Kinetics of Precipitation*. Pergamon Press Limited, Oxford.

Owens D.K. and Wendt R.C. (1969) Estimation of the surface free energy of polymers. *J. Appl. Polym. Sci.* **13**, 1741-1747.

Rabel W. (1971) Einige Aspekte der Benetzungstheorie und ihre Anwendung auf die Untersuchung und Veränderung der Oberflächeneigenschaften von Polymeren. *Farbe und Lack* **77**, 997-1006.

Rinaudo M. (2006) Chitin and chitosan: properties and applications. *Prog. Polym. Sci.* **31**, 603-632.

APPENDIX C. SUPPLEMENTARY INFORMATION FOR CHAPTER 3

C1. ADDITIONAL TABLES OF DATA

Table C.1: Summary of isotope ratio measurements shown in **Fig. 3.4**.

	$^{43}Ca/^{40}Ca$	$^{25}Mg/^{24}Mg$
Mg/Ca = 2.0		
Natural controls	0.001420	0.1262
	0.001403	0.1305
	0.001359	0.1301
	0.001387	0.1310
	0.001351	0.1271
	0.001374	0.1294
	0.001322	0.1285
	0.001333	0.1281
	0.001422	0.1275
	0.001400	0.1286
Spike controls	0.005696	0.9523
	0.005209	0.9895
	0.005646	0.9343
	0.005756	0.9424
	0.005645	0.9240
	0.005848	0.9454
	0.005764	0.9374
Transferred samples	0.001521	0.4580
	0.004691	0.9893
	0.004524	0.9800
	0.004535	1.0422
	0.004628	1.0419
Mg/Ca = 5.0		
Natural controls	0.001393	0.1255
	0.001349	0.1288
	0.001337	0.1286
	0.001268	0.1291
	0.001525	0.1256
	0.001245	0.1356
Spike controls	0.005852	1.0541
	0.005667	1.0693
	0.006247	1.0783
	0.006040	1.0801
	0.005611	1.1429
	0.005799	1.2312
	0.005609	1.1696
	0.005619	1.1841
	0.005628	1.1869
Transferred samples	0.003311	0.8820
	0.003295	0.8290
	0.001815	0.4522
	0.002387	0.6027
	0.001753	0.5496
	0.002037	0.6851
	0.002834	0.9327
	0.003232	0.8796
	0.002682	0.8865
	0.001903	0.5079

Mg/Ca = 6.0		
Natural controls	0.001320	0.1313
	0.001233	0.1348
	0.001373	0.1340
	0.001480	0.1236
	0.001481	0.1252
	0.001438	0.1189
	0.001265	0.1234
	0.001460	0.1279
	0.001448	0.1343
Spike controls	0.004150	1.0752
	0.006402	1.2553
	0.004180	1.0788
Transferred samples	0.002382	0.8101
	0.002676	0.9231
	0.001667	0.5962

C2. HYPERBOLIC BINARY MIXING MODEL

The mixing model (Langmuir et al., 1978; Vollmer, 1976) predicts the isotopic composition as different proportions of two end members are mixed together. A hyperbolic shape is produced when the end members have different Mg/Ca compositions and follows the general equation:

$$Ax + Bxy + Cy + D = 0 \qquad [C.1]$$

where x and y represent the axes in **Fig 3.4** ($^{43}Ca/^{40}Ca$ and $^{25}Mg/^{24}Mg$) and the coefficients A, B, C, and D are linear combinations of known isotopic compositions of the two end members (natural abundance ACC and spiked solution). The coefficients are given by:

$$A = {}^{24}\mathrm{Mg}_{soln}\,{}^{40}\mathrm{Ca}_{ACC}\left(\frac{{}^{25}\mathrm{Mg}}{{}^{24}\mathrm{Mg}}\right)_{soln} - {}^{24}\mathrm{Mg}_{ACC}\,{}^{40}\mathrm{Ca}_{soln}\left(\frac{{}^{25}\mathrm{Mg}}{{}^{24}\mathrm{Mg}}\right)_{ACC} \qquad [C.2]$$

$$B = {}^{24}\mathrm{Mg}_{ACC}\,{}^{40}\mathrm{Ca}_{soln} - {}^{24}\mathrm{Mg}_{soln}\,{}^{40}\mathrm{Ca}_{ACC}$$

$$C = {}^{24}\mathrm{Mg}_{soln}\,{}^{40}\mathrm{Ca}_{ACC}\left(\frac{{}^{43}Ca}{{}^{40}Ca}\right)_{ACC} - {}^{24}\mathrm{Mg}_{ACC}\,{}^{40}\mathrm{Ca}_{soln}\left(\frac{{}^{43}\mathrm{Ca}}{{}^{40}\mathrm{Ca}}\right)_{soln}$$

$$D = {}^{24}\mathrm{Mg}_{ACC}\,{}^{40}\mathrm{Ca}_{soln}\left(\frac{{}^{43}\mathrm{Ca}}{{}^{40}\mathrm{Ca}}\right)_{soln}\left(\frac{{}^{25}\mathrm{Mg}}{{}^{24}\mathrm{Mg}}\right)_{ACC} - {}^{24}\mathrm{Mg}_{soln}\,{}^{40}\mathrm{Ca}_{ACC}\left(\frac{{}^{43}\mathrm{Ca}}{{}^{40}\mathrm{Ca}}\right)_{ACC}\left(\frac{{}^{25}\mathrm{Mg}}{{}^{24}\mathrm{Mg}}\right)_{soln}$$

The model predicts the extent of mixing necessary to achieve any isotopic composition along the curve. Values for the coefficients are tabulated in **Table C.2**.

Table C.2: Hyperbolic mixing model coefficients are calculated from Mg content and isotopic composition of ACC and solution according to **Eq. C.1** and **Eq. C.2**.

Mg/Ca ratio	A	B	C	D
2	0.8879	-0.7244	0.0003340	-0.001136
5	2.1988	-1.7201	0.0006669	-0.002806
6	2.6481	-1.9263	-0.0001788	-0.003279

C3. REFERENCES

Langmuir, C.H., Vocke Jr, R.D., Hanson, G.N. and Hart, S.R., 1978. A general mixing equation with applications to Icelandic basalts. Earth and Planetary Science Letters, 37(3): 380-392.

Vollmer, R., 1976. Rb-Sr and U-Th-Pb systematics of alkaline rocks: the alkaline rocks from Italy. Geochimica et Cosmochimica Acta, 40(3): 283-295.